EINDHOVEN UNIVERSITY OF TECHNOLOGY

ARCNL
ADVANCED RESEARCH CENTER FOR NANOLITHOGRAPHY

Department of Fusion

Numerical Simulations of Droplet Impact by a Laser Pulse

Master Thesis

Maria Morbey

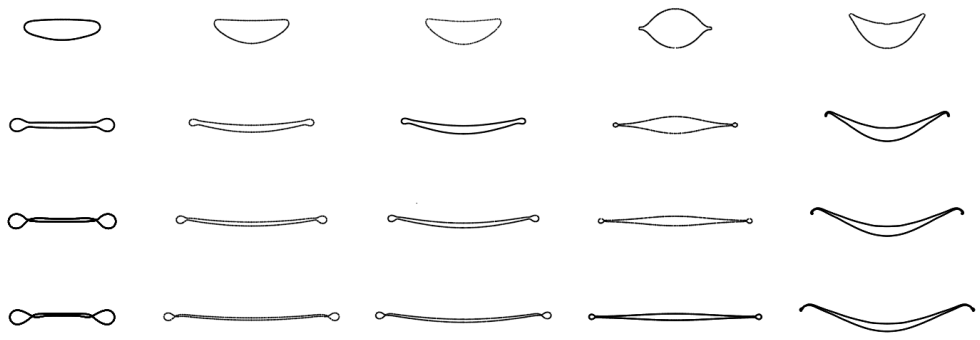

Supervisors:
B. Liu, dr. P. Rindt, dr. O. O. Versolato, prof. dr. N. J. Lopes Cardozo

Eindhoven, Monday 8th March, 2021

Abstract

In the nanolithography industry extreme ultraviolet light (EUV) is used for the fabrication of chips. To create the plasma two lasers pulses are shot at falling liquid tin droplets. The first pulse, the prepulse, propels and deforms the tin droplet into a thin sheet bounded by a rim. The second pulse, the main, pulse ablates the newly deformed target, leading to the emission of light at the required wavelength. In nuclear fusion liquid tin is considered to be a suitable candidate for the wall material in the reactor's region where highest heat loads are expected. Since nuclear fusion reactors are still a topic under research, whereas nanolithography is widely used in industry, we focus on the latter. The work done in this study can in the future be applied to fusion.

This study focuses on the fluid response of the tin droplet to different pressure profiles which are a consequence of the prepulse laser. The understanding of the droplet shape is crucial to improve the production of EUV light and minimize the production of tin fragments which contaminate the machine. For this we perform axisymmetric simulations in Basilisk, a computation fluid dynamic package. This open source package uses the Volume-of-Fluid front capturing method along side an adaptive grid. Basilisk does not simulate the laser, therefore we introduce a pressure profile on the droplet as a boundary condition. We start by validating the code and find good agreement between Basilisk simulations and theoretical models as well as experimental data and other type of simulations.

We use two type of pressure profiles, a cosine-shaped pressure profile and a Gaussian-shaped pressure profile. We start by focusing on the cosine-shaped case and change the centre-of-mass velocity that the target acquires after the pressure is exerted. The velocity change is captured in the Weber number (We$=\frac{\rho D_0 U^2}{\gamma}$) where ρ is the droplet density, D_0 is the initial droplet diameter, U is the centre-of-mass velocity, and γ is the surface tension. We track the sheet radius, sheet thickness and sheet volume. We compare our simulation data to previous analytical and empirical methods and conclude that Basilisk simulations provide an improved way to study the droplet deformation. Most striking, we observe a never seen before, increase of the sheet volume at any given time with the Weber number.

Another set of simulations is performed where the Weber number is left constant and the width of the Gaussian profile is changes. The mentioned sheet parameters are tracked. We observe an increase of the radial expansion velocity at early times which has not been reported before. A dependence of the sheet volume on the pressure profile is seen.

Basilisk does not capture the fragmentation but for most of the studied scenarios, fragmentation is not expected. The pressure profile that minimizes the mass on the edge of the target gives a high U to the liquid target and has a narrow Gaussian pressure profile. We provide a simulation tool which is ready to take any pressure profile and simulate the consequent response of the liquid.

Contents

Chapter 1

Introduction

This thesis studies a topic that overlaps with two fields, nanolithography and nuclear fusion. For those who have a general idea of these fields, it might not be obvious how the two fields overlap. While in one field going small is the goal, in the other, in the opinion of many, increasing in size is the future [1, 2]. In one field, nanometer scale structures are printed in silicium, in the other the goal is to generate Gigawatts of power in a nuclear fusion power plant. We can agree that both these fields are complex and on the cutting edge of technology. These two fields meet when it comes to materials. In both fields materials are under extreme conditions. In fusion the fuel is kept at temperatures higher than that in the sun, leading to the need of a wall that can handle unprecedented heat and particle fluxes [3]. In nanolitography the need for a high-intensity source of short-wavelength light calls for extreme solutions. The solution found was the interaction between a laser and liquid tin [4]. In fusion, one of the solutions being considered for the region where the particle and heat fluxes are highest is to use liquid tin [5]. A possible drawback of this solution is the ablation of tin and the possibility of splash and contamination of the plasma. In the present nanolithography machines droplets of tin are hit in free fall by an intense laser pulse. This creates a tin plasma which radiates in the desired wavelength range. But here, too, the interaction between the tin fluid and the plasma needs to be understood in order to optimise the generation of short-wavelength light and to reduce the ejection of fragments that contaminate the optical components in the machine. Thus, the overlap of the two fields is very concrete. Even though these problems have similarities, they present differences. These include the time and length scales, which in nuclear fusion are around 10^4 and 10^6 times bigger than in nanolitography, respectively [6, 4]. However, since the physics of the interaction of the high heat loads with the tin fluid, and the subsequent dynamics of the tin is dominated by hydrodynamics, it is scale invariant. In other words, what we learn in one field can be applied on to the other. In this case, since fusion power plants do not yet exist whereas nanolithography is well developed, the strategy is to learn from the nanolithography with the aim to design better fusion power plants. Below, we will first present the background of the use of tin in nanolithography and fusion reactors, respectively, and subsequently formulate a research question in line with the approach presented above.

1.1 Nanolitography

Nanolithography is the process of etching, writing and printing patterns at the nanometer scale. Chips production used nanolitography techniques. Chips are essential components of electronic devices, such as a mobile phone. In the heart of these chips are the transistors. To improve the chips' performance without increasing its size, the semiconductor industry has decreased the transistor size to tens of nanometers. For comparison, the thickness of a hair is around 40000 nanometers. The number of transistors on a microelectronic chip doubles every year, following Moore's law [2]. Sustaining this increase remains a challenge in the semiconductor industry. One of the critical processes is photo lithography [7].

We start with a wafer covered by a photoresist. The wafer is exposed to light through a mask. This mask, often called reticle, is imaged onto the photoresist after being reduced in size. Depending on the type of photoresist, negative or positive, the part exposed to the light becomes soluble and it is etched away, or the non exposed part is etched away, respectively. This process is repeated for the same wafer using different masks. The achievable resolution of this process scales proportionally with the wavelength of the light [8]. As such, the smaller the wavelength, the better is the resolution. Nowadays, in latest generation of lithography devices the light used has a wavelength of 13.5nm, in the extreme ultraviolet range, EUV [9].

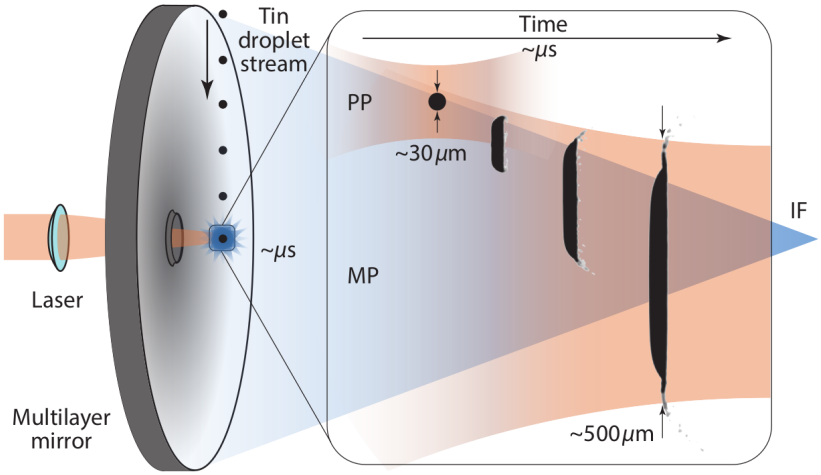

Figure 1.1: Simplified scheme of laser-droplet interaction in nanolitography machines. First, spherical tin droplets are hit by a prepulse laser (PP). Consequently, the droplet are propelled and reshaped into a more suitable target for the main-pulse laser irradiation (MP). Due to the high energy of the main plasma tin plasma is created and EUV is emitted. Figure from [4].

The EUV light source makes use of the interaction between a tin droplet and a laser. After a powerful enough laser impact the tin ablates and goes into the state of plasma. This highly ionised plasma emits light with a spectral peak at 13.5nm. First, the EUV light is collected by a multilayer collector mirror, which reflects the light to the all other optical components. These tools redirected the EUV light to the reticle, which images it to the the wafer with the photoresistor layer. In each optical tool, part of the energy is reflected, but not all, which reduces the amount of light used for nanolithography.

A challenge faced by the lithography community is the ejection of neutral and ionised tin fragments from the liquid target. These fragments, if deposited in the optical components, lead to a loss of reflectivity and decrease of the amount of useful light [10]. This is especially a problem in the collector, Fig. 1.1. Its proximity to the light source makes it the most affected. To reduce the degradation of optical components by tin deposition, it was chosen to introduce only a limited amount of tin per time in the machine. A laser shoots falling liquid tin droplets coming from a tin jet. The droplets are created with a constant repetition rate and the same size characteristics, Fig. 1.1. Since a spherical tin target is not the shape that results in the most emitted light, a less intense laser is fired to re-shape the target into a disk before the main pulse. This is the prepulse laser. The prepulse laser has a duration of a few tens of nanoseconds, and it has just enough intensity to ablate a small fraction of the tin mass, leading to the plasma creation. This plasma applies pressure on the droplet, which undergoes a deformation. This newly deformed target is considered a more suitable target for the main CO_2 laser pulse. This target is characterized by a sheet which is bounded by a rim. The rim is the thicker edge perimeter. At the moment, a 10 μm wavelength of tens of nanoseconds laser is used for the pre-pulse [4]. In general, these laser pulses result in an ablation pressure, p_e with a duration of τ_e which are usually assumed to allow to describe the droplet deformation as that of an incompressible fluid [11]. Previously to the research of droplet impact by a laser, droplet impact on a pillar had been extensively studied. These two phenomena present a similar enough behaviour that allows for the theory of the droplet impact on a pillar to be applied to the impact of a laser in a droplet [12, 13, 14, 15]. So far the research in the field of a laser impact on a droplet has been done using both simulations and experiments. Even though several studies have been performed, there are still unanswered questions, such as what is the thickness profile and consequent mass distribution. A good understanding of the droplet's mass distribution after the pressure field is crucial for the advancement of EUV machines [14]. By estimating the amount of tin mass retained in the expanding target, we understand and reduce the fragmentation, allowing us to extend the lifetime of the optical tools and increase the amount of tin used to create EUV light.

1.2 Nuclear Fusion

Fusion is a clean energy source under research. This clean energy source has several advantages, its independence of the weather, fuel abundance, and it does not produce long-lived nuclear waste [16]. In a fusion reactor, the fuel is in the state of plasma, at around 100 million Kelvin. No material can handle this temperature, so a magnetic cage is used to keep the plasma in place, preventing wall damage and cooling down of the core plasma by contamination. In a fusion reaction, two hydrogen isotopes fuse together resulting in helium (He), and neutrons. Around 80% of the energy is carried out by neutrons which go through the walls to a blanket around the magnetic cage where they deposit their energy. The other 20% are carried by the alpha particles which heat the fuel and keep the reaction going [17]. These particles will eventually reach the outer part of the plasma. Once they have reached it, they will follow the magnetic field lines to the bottom of the reactor, where the divertor is located. This magnetic configuration leads to very local deposition of heat and particles, demanding the target material to withstand conditions never seen before [5].

It is expected for future fusion power plants that plasma instabilities named ELM, edge localised mode, can deposit up to 10 GW/m^2 in the divertor. No solid material is able to withstand the extreme conditions [18], so the fusion community is leaning towards a different path, liquid metal divertors, LMD [3]. Like the semiconductor industry, fusion is considering liquid tin as a plasma facing material. This is where both fields overlap.

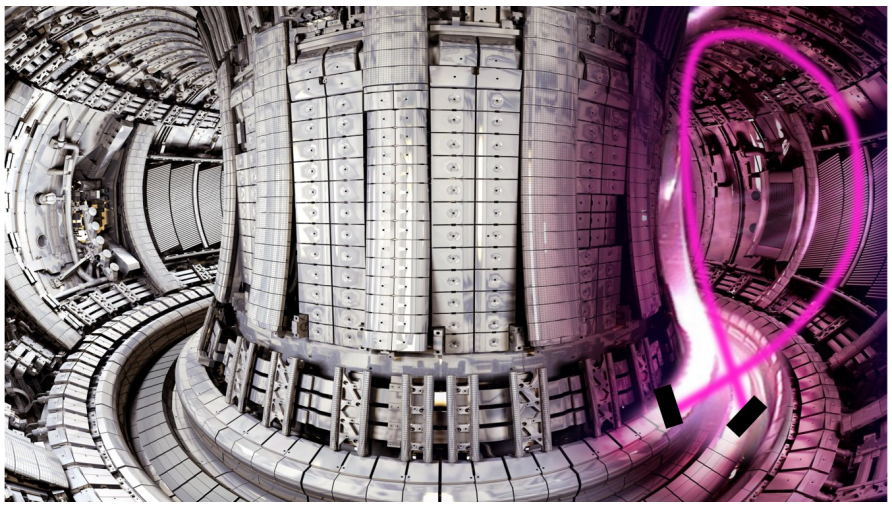

Figure 1.2: Inside view of a tokamak with the Last Closed Flux Surface (LCFS) schematically shown in pink and in black the divertor targets. Where the LCFS meets the divertor targets is called the Strike point. The strike point is the point which is subject to highest heat loads and particle fluxes. Figure adapted from [5].

1.3 Research Question and Plan

In this thesis, we focus on the nanolithography application. The shape acquired by the droplet depends not only on the laser's energy but also on its shape, focus conditions. The goal of this thesis is to, through simulations, give more insight on droplet shape properties that experiments can not provide and deliver a code that can guide future experiments. The research question is

What is the time evolution of the mass distribution of a droplet after a laser impact?

The research question is evaluated by conducting numerical fluid dynamic simulations in Basilisk, an open-source package that solves the incompressible Navier Stokes in an axisymmetric setup. The fluid edge over time is provided from these simulations, and the volume, thickness, and radius can be tracked. We perform a scan of pressure profiles and Weber numbers (We$=\frac{\rho D_0 U^2}{\gamma}$). Where ρ and γ are the density and the surface tension of the liquid, respectively, D_0 and U are the initial droplet diameter and the propulsion speed, respectively. The various Weber reflect the change of the propulsion speed of the droplet. The obtained results are compared to both experimental data and theoretical models. In fluid dynamics, scientists usually use dimensionless parameters. This allows the simulation to have the same dimensionless parameters but different specific

configurations, making the simulation more time effective. These will be the first simulations of laser impact on a droplet ever done in Basilisk. The stat-of-the-art research so far has made use of Boundary Integral, BI, simulations but it has not yet accomplished long period simulations and has not investigated detailed sheet properties or changes in the Weber number. The simulation time is limited by early fragmentation because viscosity effects are not taken into account [19]. Basilisk is able to take viscosity into account which, in principle, would improve this numerical artefact. Consequently, longer times periods can be simulated when using Basilisk. In addition, we will discuss more sheet details, therefore providing new insights.

1.4 Scope: Nanolithography and Nuclear Fusion

The scope of this thesis goes beyond nanolithography and also includes nuclear fusion. If we can have a code that predicts a droplet's behaviour after a laser impact, we can modify it in a way that indicates how the bath of liquid tin in the divertor will behave under extreme heat loads. This is not directly studied in the thesis due to since there is no analytical expression of the pressure profile created by a laser impact onto a liquid pool. We can, however, use toy models to estimate the simulation capacities in this specific case. There is almost no literature on laser ablation on a pool of tin, but it is believed that the phenomenon is somewhat similar to the droplet impact on a pool. Experiments have been conducted on this in Ref. [20], but there is no droplet impact data that is directly comparable, so we simulate a droplet impact on a pool with the same parameters and track the studied parameters such as crown height and width to see if indeed the droplet impact theory could be used in the ELM/laser pool impact world.

In summary, this work should provide more information on the droplet's fluid dynamic response after the laser pulse impact and open the door to the exploration of the effects of heat loads on a liquid metal divertor. This project is done in collaboration with the Fusion and Applied Physics department of TU/e and ARCNL, the Advanced Research Centre for Nanolithography. This collaboration results in a strong team with competences in all fields involved, fusion, nanolithography, and computational fluid dynamics.

1.5 Structure

This thesis is structured as follows. In chapter 2 we present the theoretical background for several varieties of droplet impacts: droplet impact on a pool, droplet impact on a pillar, and droplet impact by a laser. In this chapter, we also go through the used Basilisk solvers and its methods. We start with the Navier-Stokes equation and the used assumptions, discussing the volume-of-fluid method used and the adaptive mesh refinement. In chapter 3 we discuss the validation of the code for droplet impact onto a pool and laser droplet impact. In addition, we describe the sensitivity tests performed. In chapter 4 we show the difference between several Weber numbers with the pressure profile shape in terms of the radial expansion, mass distribution, and thickness are studied and compared to models. In chapter 5 we follow the same parameters for different pressure profile widths but same Weber number. In chapter 6 we review and discuss the results from chapters 4 and 5 as well as their implications for fragmentation. Moreover, the range of validity of the simulation and the link between the laser and the pressure profiles are discused. In chapter 7 summary and an outlook on future directions of the present simulations are suggested. In chapter 8, conclusions are stated.

Chapter 2

Literature study

In this chapter, we provide theoretical background from prior studies, which in the following chapters will be used to interpret our numerical results and enable their comparison to the literature. First, in section 2.1 the hydrodynamic non-dimensional numbers, such as the Weber number and Bond number, are introduced. Second, in section 2.2, in addition to the laser impact on a droplet, we introduce the cases of droplet impact on different substrates, e.g., liquid pool and pillar. In particular, the case of droplet-pillar impact and its relevant models from the previous studies will be detailed (subsection 2.2.2). Regarding the main focus of this thesis, in subsection 2.2.3 we review literature about the effect of the laser on a liquid droplet. Finally, in section 2.4 we give a brief introduction to Basilisk.

2.1 Dimensionless parameters in Fluid Dynamics

Dimensionless numbers are widely used when interpreting results in fluid dynamics, . This allows for the comparison of the same phenomena for different initial conditions and liquids. The relevant dimensionless number used in this thesis are the Weber number, We, which compares inertia to surface tension; Reynolds number, Re, which compares inertia to viscosity effects; and the Bond number, which compares gravity to surface tension. They are defined as follows:

$$\mathrm{We} = \frac{\rho D U^2}{\gamma}, \quad \mathrm{Re} = \frac{\rho D U}{\mu}, \quad \mathrm{Bo} = \frac{\rho g D^2}{\gamma}. \tag{2.1}$$

Where ρ is the density, μ the viscosity, γ the surface tension of the liquid, and g the gravitational constant. D is the characteristic length scale, and U the characteristic velocity scale.

Besides the comparison between forces and effects, it is also important to review the dimensionless times. They are named inertial time, τ_i, and capillary time, τ_c. The first, τ_i, takes into account D and U, while τ_c accounts for the surface tension and characteristic length.

$$\tau_i = \frac{D}{U}, \quad \tau_c = \sqrt{\frac{\rho R^3}{\gamma}}, \tag{2.2}$$

where $R = D/2$.

2.2 Several scenarios of droplet impact

In this section we present the theory for three different types of the droplet impact starting with the droplet impact on a pool, insubsection 2.2.1. Secondly, we discuss the droplet impact on a pillar, in subsection 2.2.2, and lastly we introduce the laser impact on a droplet, in subsection 2.2.3.

2.2.1 Droplet impact onto a pool

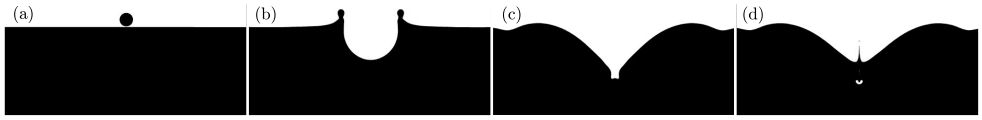

Figure 2.1: Basilisk simulation images of the time lapse of droplet impact onto a pool where D_0=0.04, U=1, We=500 and Re=1000. a) The droplet starts at an initial distance of 0.1D_0 from the pool level. b) When it hits the pool the liquid will start moving radially originating a crown and a cavity. c) As time evolves the crown becomes thicker and the cavity less round and more deep. d) Once the capillary waves collapse a jet may be formed [21, 22, 23].

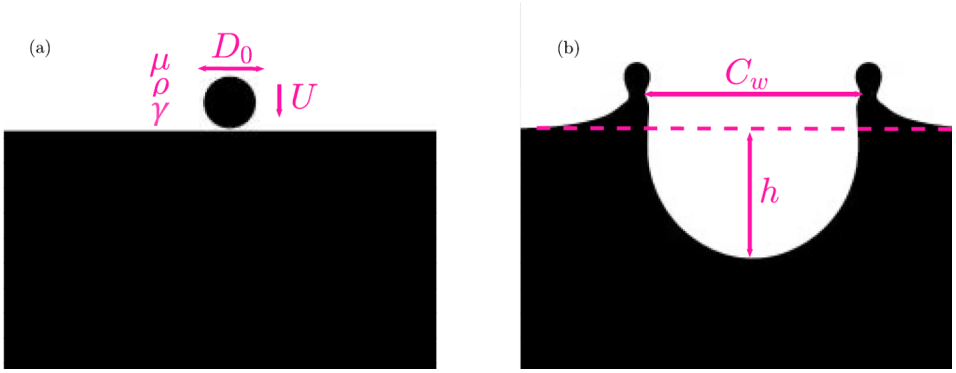

Figure 2.2: Definition of the maximum cavity depth, h, crown width, C_w, in this work, for a droplet impact onto a pool. Images from our Basilisk simulation. a) Droplet falling into the pool with Diameter, D_0, density ρ viscosity μ and surface tension γ. b) After the impact a cavity is generated, with a height h, defined as the distance between the initial impact point to the deepest point of the cavity. Above the initial surface a crown is form with a width defined as the distance between the two indentations, C_w [21, 22].

When a droplet impacts on a pool, the resting liquid is set into motion, and its dynamics are mainly determined by the Weber number. In this event, U is the velocity of the droplet when it reaches the pool and D_0 is the initial droplet diameter, see Fig. 2.2 [21]. In the beginning, there is a competition between the inertial forces that want to set the liquid into motion and the surface tension which wants to keep the liquid together and at the minimal energy state. The higher the velocity compared to the surface tension (measured by the Weber number), the more violent is this flow. For sufficiently high Weber numbers, we see a cavity forming, from where liquid is pushed away, and a crown, where the liquid is above the initial height, see Fig. 2.1 [21]. For scenarios where gravity can be neglected as well as the viscosity, Refs. [23, 24] show the influence of the Weber number on the maximum cavity depth, h_m.

By multiplying the surface tension by the area of the cavity, we obtain the energy required to have the extra surface of the cavity. In this case, we take h_m as the characteristic length [24].

$$E_\gamma \sim \gamma h_m^2. \tag{2.3}$$

If Bo $\ll 1$, gravity can be neglected. Therefore, the initial energy is only the kinetic energy. We can replace in place of E_γ

$$\rho U^2 D_0^3 \sim \gamma h_m^2. \tag{2.4}$$

Rearranging the terms and keeping in mind the Weber number definition we get:

$$\frac{h_m}{D_0} \sim \mathrm{We}^{1/2}. \tag{2.5}$$

We will verify this relationship by simulating the droplet impact onto a pool in Basilisk with a range of Weber numbers.

The penetration depth of the cavity initially increases with an approximately constant velocity. If the pool and droplet have the same density, this velocity is weakly dependent on the reaming liquid properties and its value is approximately $1/2U$ [25, 26, 27]. This means that the cavity depth of D_0 is reached at $t = 2U/D_0$. We will show that our Basilisk simulation agree with the mentioned penetration velocity.

2.2.2 Droplet impact onto a pillar

Droplet impact onto a pillar has been extensively studied. In this type of impact, U is defined as the speed with which the droplet impacts on the pillar and D_0 is the initial droplet impact. When a droplet impacts on a pillar, the pillar suffers no alteration. This phenomenon is similar enough to the droplet impact by a laser that we can use the theory of droplet impact on a pillar for the laser impact on a droplet [12, 14, 28]. Namely, in the reference frame of the droplet, the pillar impacts the droplet in a very similar way as the pressure field created by a laser does. Important sheet characteristics are its thickness, h and its radial length R.

A theoretical expression for the sheet radial expansion, R, after a droplet impact on a pillar, is given by [29]. Figure 2.3 shows an example of this impact. With the droplet D_0 and sheet h and R highlighted.

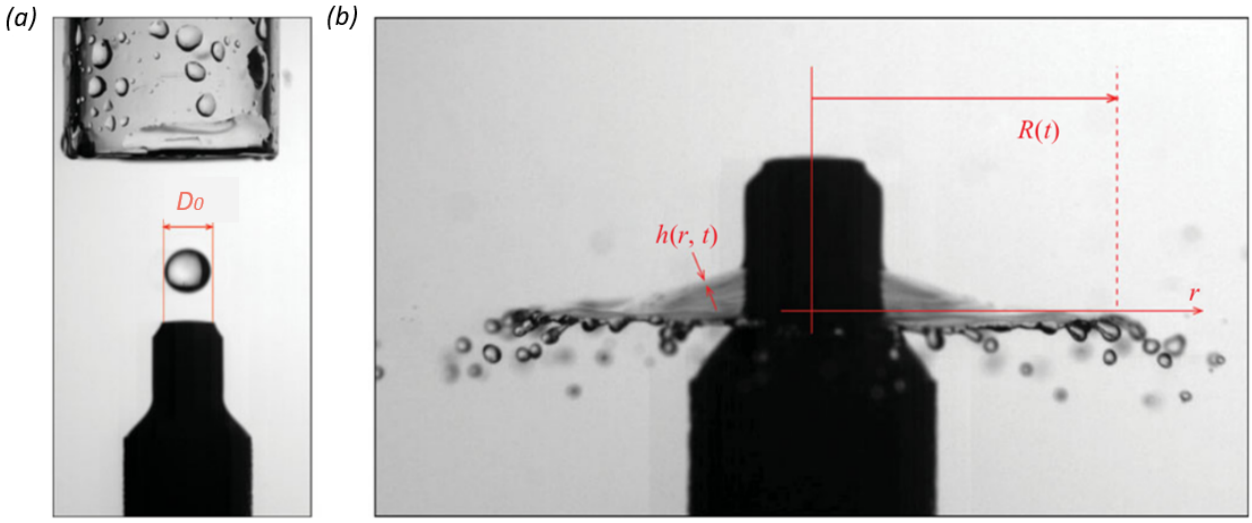

Figure 2.3: (a) A water drop just before it impacts a pillar with the same diameter. (b) Side view of the expanding sheet and definitions of the sheet thickness $h(r,t)$ and radius $R(t)$. Figure from [29].

This model comes from the inviscid and incompressible Navier-Stokes equation (Euler equation) assuming a sheet with a slender-slope shape. To solve the Euler equation, Ref. [29] seeks a solution based on the solution previously found for an continuously impacting jet from Ref. [30], which is given by:

$$h(r,t) = \frac{f(t)}{r}, \tag{2.6}$$

where $f(t)$ is an unknown fucntion of time. After assuming the sheet expansion rate within the pillar radius to be zero the following relation is reached:

$$f(t)[R(t) - R_0] = \frac{\frac{\pi D_0^3}{6}}{2\pi}\left(1 - \frac{t}{\tau_{cv}}\right)^2, \tag{2.7}$$

where $\tau_{cv} = \sqrt{\frac{\rho D_0^3}{6\gamma}}$, R(t) is the sheet radius and R_0 is the initial droplet radius. Ref. [29] derives the following R(t) expression:

$$\frac{R(t) - R_0}{R_0} = \sqrt{\frac{\rho u^2 R_0}{\gamma}}\frac{t}{\tau_c}\left(1 - \frac{\sqrt{3}}{2}\frac{t}{\tau_c}\right)^2, \tag{2.8}$$

Combining Eqs. (2.8), (2.6) and (2.7) we obtain:

$$h(r,t) = \frac{D_0^3}{12rtu}. \tag{2.9}$$

From this model's radial expansion, the volume expected in the sheet can be derived, which is given by [31]:

$$\frac{V_{sheet}}{V_0} = \frac{1}{V_0}\int_{R_0}^{R(t)} 2\pi r h(r,t) dr = \left(1 - \frac{\sqrt{3}}{2}\frac{t}{\tau_c}\right)^2, \tag{2.10}$$

where V_{sheet} is the sheet volume and V_0 is the initial volume of the droplet. In the rest of this thesis we refer to these expressions from Ref. [29] as Model 1.

Droplet-pillar impact has also been studied by in Ref. [32]. In their work, a self-similar solution to describe the the thickness profile of the sheet has been developed. It is assumed that the flow is inviscid and the curvature-induced radial pressure gradients can be neglected in the sheet. The flow in the sheet is described by the axisymmetric Euler equation

$$\frac{\partial u_r}{\partial t} + u_r \frac{\partial u_r}{\partial r} = 0, \tag{2.11}$$

indicating that expanding sheet flow is $u_r(r,t) = r/t$. The self-similar solution found is:

$$h(r,t) = \frac{1}{t^2}\psi\left(\frac{r}{t}\right). \tag{2.12}$$

In dimensionless variables, it is given by

$$h^* {t^*}^2 = F\left(\frac{r^*}{t^*}\right), \tag{2.13}$$

where $r^* = r/D_0$, $h^* = h/D_0$, $t^* = Ut/D_0$ are the self-similar variables and $F\left(\frac{r^*}{t^*}\right) = \frac{U^2}{D_0^3}\psi\left(\frac{r}{t}\right)$. This equation implies that the sheet thickness can be described by one universal curve when using the self-similar variables. This is a reciprocal polynomial and its coefficients are to be obtained from fitting the unified self-similar solution to data. We refer to this model as Model 3. In the next subsection we introduce a model which describes also the radial expansion and we will name it Model 2.

2.2.3 Droplet impact by a laser

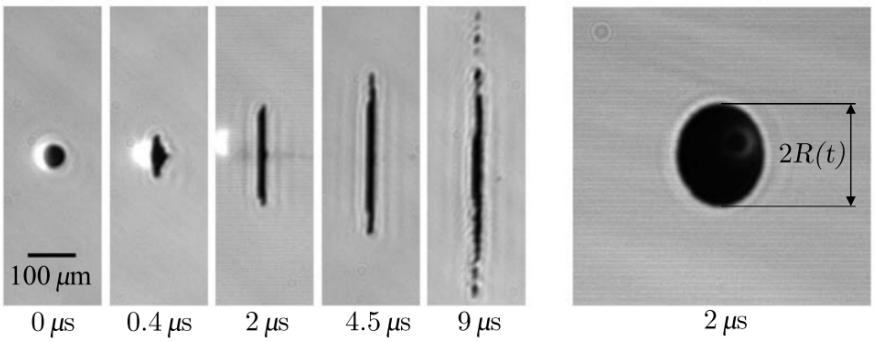

Figure 2.4: Shadowgraphy images of In-Sn droplets in side and front view. Expansion of an In-Sn droplet as viewed from the side. Droplet impact by 10-ns Nd:YAG laser pulse from the left. Figure from [4].

As introduced before, in nanolithography, to produce EUV light a laser is shot onto a liquid tin droplet which will be deformed into a expanding sheet. Later on, a second laser pulse, the main pulse, ablates the deformed droplet to emit the EUV light needed. The first prepulse laser ablates a small fraction of the mass leading it to the plasma state. The plasma expands away from the droplet surface on a time τ_a, the lifetime of the plasma. The generated plasma exerts pressure on the droplet which undergoes a deformation. Figure 2.4 shows the time evolution of the droplet seen in experiments. In this thesis, we focus solely on the fluid dynamics part. The time scale of the fluid response and the plasma in increasing order is as follows:

$$\tau_\mathrm{p} < \tau_\mathrm{a} \ll \tau_\mathrm{i} < \tau_\mathrm{c}, \tag{2.14}$$

where, $\tau_\mathrm{p} \approx 10^{-8}s$, is the laser pulse time, τ_a is the lifetime of the generated plasma, which is a few times τ_p, $\tau_i \approx 10^{-4}s$, is the inertial time, and $\tau_c \approx 10^{-3}s$, is the capillary time, [4, 13, 33, 34]. This ordering of the time scales illustrates how the plasma generation $(\tau_\mathrm{p}, \tau_\mathrm{a})$ can be separated from the fluid-dynamic response

(τ_i, τ_c). The separation of time scales allows for the study of each part separately. In this thesis we focus on the fluid dynamic response of the droplet. The pressure exerted by the plasma is used as a boundary condition.

Calculation of the initial velocity field from an arbitrary pressure profile

Following the work from Ref. [13] we start with the incompressible flow Navier stokes equation,

$$\frac{\partial \mathbf{u}}{\partial t} + (\mathbf{u} \cdot \nabla)\mathbf{u} - \nu \nabla^2 \mathbf{u} = -\nabla w + \mathbf{g}, \tag{2.15}$$

where $\mathbf{u}$ is the characteristic velocity, $\nu = \frac{\mu}{\rho}$ is the kinematic viscosity and $w = \nabla\left(\frac{p}{\rho}\right)$ is the gradient of the pressure, p. Since the Reynolds number is rather large in this kind of set up we can assume that the flow is inviscid. The negligible gravity can be interpreted as Bo $\ll 1$. If the drop does not deform on the time scale of the pressure pulse, we can say that $\partial \boldsymbol{u}/\partial t \gg (\boldsymbol{u} \cdot \boldsymbol{\nabla})\boldsymbol{u}$. Assuming incompressibility the velocity filed right after the pressure pulse is obtained as

$$\boldsymbol{u} \approx -\frac{\tau_p}{\rho} \nabla p, \tag{2.16}$$

where $\boldsymbol{u}$ is the velocity and p is the time-average pressure inside the droplet. In Fig. 2.5 we see a sketch of the problem geometry.

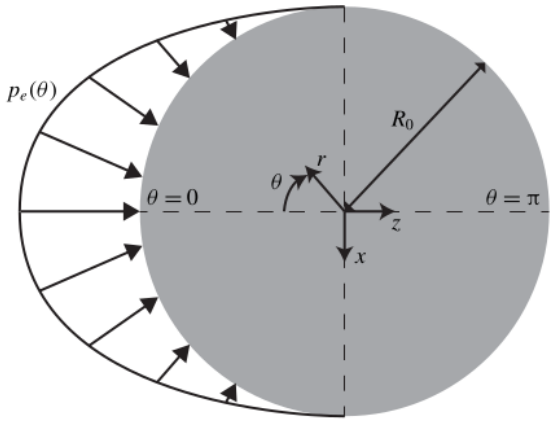

Figure 2.5: Axisymmetric pressure pulse $p_e(\theta)$ applied on the surface of a droplet with radius R_0. Spherical (r,θ,ϕ) and Cartesian (x,y,z) coordinates are indicated. Sketch from [13].

From here on, as in Ref. [13], we use scaled variables, radial coordinate r/R_0, pressure p/p_e, velocity $\rho R_0 u/p_e \tau_p$ and time t/τ_p, where p_e is obtained from the laser energy. The dimensionless pressure can be decomposed into Legendre polynomials P_ℓ for any laser-beam profile

$$p(r, \theta) = \sum_{\ell=0}^{\infty} A_\ell r^\ell P_\ell(\cos\theta), \tag{2.17}$$

with coefficients

$$A_\ell = \frac{2\ell + 1}{2} \int_0^\pi f(\theta) P_\ell(\cos\theta) \sin\theta d\theta, \tag{2.18}$$

where $f(\theta) = p(1, \theta)$ is the pressure on the droplet surface normalized such the axial momentum is one, i. e.,

$$\frac{4}{3}\pi U = 2\pi \int_0^\pi f(\theta) \cos\theta \sin\theta d\theta = 1. \tag{2.19}$$

A_1 is the dimensionless droplet centre-of-mass velocity, U. This means that U is always the same, independently of the pressure profile. In the laser droplet impact case U is defined as the propulsion speed in the laser directions and D_0 is the initial droplet diameter, before the droplet is hit the laser.

As shown in Eq. (2.19), the pressure profile exerted on droplet interface $f(\theta)$ is the pertinent input to determine the velocity field in the droplet using Eq. (2.16). In this work, we take $f(\theta)$ as Gaussian or cosine shaped pressure profile . The cosine shaped pressure profile on the droplet surface is obtained from the

projection of a uniform laser-beam profile. Applying the mentioned pressure profile leads to a sheet that is symmetric around the mid-plane perpendicular to the laser direction. In other words, when a cosine-shaped pressure profile is applied on one side of the droplet, it is observed the same behaviour as if two identical pressure profiles were applied on opposite sides of the droplet. The complete expression of $f(\theta)$ for both of these two profiles are elucidated in Ref. [13]. From their study, the Gaussian angular profile of the pressure boundary condition is given by:

$$f(\theta) = c \exp\left[-\theta^2 / \left(2\sigma^2\right)\right], \tag{2.20}$$

where σ is a measure for the width of the pulse, and c is such a prefactor that satisfies Eq. (2.19), which is a sole function of σ and angular coordinate. As for the cosine boundary condition $f(\theta)$ is given by:

$$f(\theta) = \frac{3}{2\pi} \cos\theta H(\pi/2 - \theta). \tag{2.21}$$

In this equation, H is the Heaviside function which restricts the interaction between the pressure pulse and the droplet to one side. The velocity can be obtained from Eq. (2.16). It is important to stress that regardless of the specific form of $f(\theta)$, Eqs. (2.17), (2.18) and (2.19) are always true.

Radial Expansion and Sheet Thickness Model

A model for the radial expansion of a laser onto a droplet is given by Ref. [13] we call this model, Model 2:

$$\frac{R(t) - R_0}{R_0} = \frac{\cos\left(\sqrt{3}\frac{t}{\tau_c}\right) + \sqrt{\frac{2}{3}}\sqrt{\frac{E_{k,d}}{E_{k,cm}}}\sqrt{\frac{\rho u^2 R_0}{\gamma}} \sin\left(\sqrt{3}\frac{t}{\tau_c}\right) - R_0}{R_0}, \tag{2.22}$$

where $\frac{E_{k,d}}{E_{k,cm}}$ is the energy partition and accounts for the energy received by the droplet that goes into the droplet translation and to the radial deformation. $E_{k,cm}$ is the translation kinetic energy and $E_{k,d}$ is the defined as the deformation kinetic energy of the droplet, while E_k is the total kinetic energy. E_k is the sum of $E_{k,d}$ and $E_{k,cm}$. The energy partition value depends on the shape of the pressure profile. For the cosine-shaped pressure pulse $\frac{E_{k,d}}{E_{k,cm}} = 0.35$.

This radial expansion model assumes a uniform disk thickness profile. Therefore, based on the mass conservation the thickness of the sheet is given by:

$$h = 4/3R(t)^{-2}, \tag{2.23}$$

where $R(t)$ is determined by Eq. (2.22).

Instabilities

The capillary instabilities manifest mainly in breakup holes along the sheet, and the formation of fragments occurring at the edge of the sheet. Hole nucleation is believed to be caused by the roughness of the beam profile due to thermal noise and by initial surface roughness [35]. The acceleration of the droplet, due to the plasma, amplifies the mentioned initial noise. In addition, the sheet becomes thinner and rupture eventually happens. These holes seem only to appear when $R/R_0 \approx 6$. Central sheet holes start in the middle and travel outwards, they only start influencing the fluid dynamics when they are close to the rim. In the rim, corrugations are seen. They are the result of the competition between the surface tension pulling the rim inwards and a fictitious force pushing the liquid outwards due to the deceleration, illustrated in Fig. 2.6. Due to the corrugation, ligaments form and eventually, these ligaments break into fragments. As seen in Fig. 2.6 this phenomena leads to thicker and thinner parts in the rim [36].

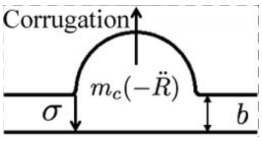

Figure 2.6: Schematic view of a corrugation formation. Figure from [36].

2.3 Summary of the models

In this section we show a table with all the three models to facilitate the reading of this report. In Tab. 2.1 we show the models' radial expansion and sheet expansion expressions. In the last column it is indicted the impact type which the model was initially derived for.

		Analytical Expression		
	Ref.	Radial expansion	Sheet thickness	Impact type
Model 1	[29]	$\frac{R(t)-R_0}{R_0} = \sqrt{\frac{\rho u^2 R_0}{\gamma}}\frac{t}{\tau_c}\left(1-\frac{\sqrt{3}}{2}\frac{t}{\tau_c}\right)^2$	$h(r,t) = \frac{D_0^3}{12rtu}$	Pillar
Model 2	[13]	$\frac{R(t)-R_0}{R_0} = \frac{\cos\left(\sqrt{3}\frac{t}{\tau_c}\right)+\sqrt{\frac{2}{3}}\sqrt{\frac{E_{k,d}}{E_{k,cm}}}\sqrt{\frac{\rho u^2 R_0}{\gamma}}\sin\left(\sqrt{3}\frac{t}{\tau_c}\right)-R_0}{R_0}$	$h = \frac{4/3}{R(t)^2}$	Laser
Model 3	[32]	-	$h(r,t) = \frac{1}{t^2}\psi\left(\frac{r}{t}\right)$	Pillar

Table 2.1: Models summary

Model 3 only presents a universal sheet thickness, Eq. (2.13). In Ref. [32] Model 3 was used for droplet on a pillar impact experiments. The ansatz taken is

$$F(x) = \frac{1}{a_3x^3 + a_2x^2 + a_1x} \tag{2.24}$$

where $x = \frac{r^*}{t^*}$. Several coefficient values (a_3, a_2, a_1) where found depending on the ratio between the droplet diameter and pillar diameter, η, used in the experiments. The case where $\eta = 1.9$ is chosen to compare to the Basilisk simulations, explanation is given chapter 4. The coefficients found in Ref. [32] by fitting Eq. (2.24) to the experimental data for $\eta = 1.9$, result in the following expression:

$$F(x) = \frac{1}{18x^3 - 30x^2 + 35x}. \tag{2.25}$$

We refer to it as curve from Wang *et al.*. In Ref. [31] Model 2 was also used. In this case it was fitted to data from laser impact on a droplet. The ansatz taken was:

$$F(x) = \frac{1}{a_1x^2 + a_1x + a_0}. \tag{2.26}$$

This expression was fitted to experimental data with a Weber number range We=4000-40 000 with droplet diameters of $D_0 = 32\mu$m and $D_0 = 26\mu$m, impacted by a laser beam focused to a Gaussian spot of 105μm FWHM. The curve obtained in Ref. [12] is:

$$F(x) = \frac{1}{-2.5x^2 + 6.93x + 1.65}. \tag{2.27}$$

In chapter 4 we will also use this expression using variables with dimensions:

$$h(r,t,U,D_0) = \frac{D_0^3}{1.65U^2t^2 + 6.93Utr - 2.5r^2}. \tag{2.28}$$

We refer to these equations from Ref. [12] as curve from Liu *et al.*.

2.4 Basilisk

In this section, we describe Basilisk, the open-source numerical solver for the partial differential equations. Axisymmetric simulations with an adaptive Cartesian mesh are performed to solve the incompressible Navier-Stokes equations. We start by explaining how Basilisk discretizes the Navier-Stokes equations, which is followed by the introduction of the method volume of fluid (VoF) method to capture the interface and the adaptive refinement.

2.4.1 Incompressible Navier-Stokes Solver

In this work we will conduct an axisymmetric simulation of a two-phase incompressible fluid. The flow is governed by the Navier-Stokes equation and the continuity equation. In our current study Bo $\ll 1$ so gravity can be neglected. The Navier stokes equation for incompressible fluids and the continuity equation are given by:

$$\rho\left(\partial_t \boldsymbol{u} + \boldsymbol{u}\cdot\boldsymbol{\nabla}\boldsymbol{u}\right) = -\nabla p + \mu\Delta\mathbf{u} \tag{2.29}$$

$$\nabla\cdot\mathbf{u} = 0 \tag{2.30}$$

The time discretization in Basilisk is done by means of the projection method. The time-splitting projection method was introduced by Alexandre Chorin in 1967 [37].

We here illustrate a simple case of the projection method, with constant ρ [38, 39, 40]. The first step is to discretize Eq. (2.29)

$$\frac{\mathbf{u}^{n+1}-\mathbf{u}^n}{\Delta t} + \left(u^n\cdot\nabla\right)\cdot\mathbf{u}^n = \nu\nabla^2\mathbf{u}^n - \frac{1}{\rho}\nabla p^{n+1} \tag{2.31}$$

where $\mathbf{u}^n$ and ν are the the velocity at n^{th} time step and the kinematic viscosity, $\nu = \frac{\mu}{\rho}$. The final solutions are $\mathbf{u}^{n+1}$ and p^{n+1}, the pressure and the velocity in the next time step, respectively. In the projection method used in Basilisk, the pressure term is simply omitted, leading to the complete decoupling of the intermediate velocity field, $\mathbf{u}^*$.

$$\frac{\mathbf{u}^*-\mathbf{u}^n}{\Delta t} = -\left(\mathbf{u}^n\cdot\nabla\right)\mathbf{u}^n + \nu\nabla^2\mathbf{u}^n, \tag{2.32}$$

where $\mathbf{u}^*$ is an intermediate velocity that does not obey to the divergence-free condition, Eq. (2.30). The pressure term is then reintroduced

$$\mathbf{u}^{n+1} = \mathbf{u}^* - \frac{\Delta t}{\rho}\nabla p^{n+1}. \tag{2.33}$$

This pressure is calculated in a way that $\mathbf{u}^{n+1}$ satisfies the continuity equation:

$$\nabla\cdot\mathbf{u}^{n+1} = 0. \tag{2.34}$$

Consequently we have that:

$$\frac{\rho}{\Delta t}\left[\nabla\cdot\mathbf{u}^{n+1} - \nabla\cdot\mathbf{u}^*\right] = -\nabla^2 p^{n+1}. \tag{2.35}$$

Resulting in the Poisson equation:

$$\nabla^2 p^{n+1} = \frac{\rho}{\Delta t}\nabla\cdot\mathbf{u}^*. \tag{2.36}$$

Besides the time discretization, spatial discretization is also of great relevance. Basilisk uses a staggered mesh which uses centre cells values and auxiliary face values. First, the face velocity values are computed. After the pressure correction is determined the cell-centre velocity field is determined. Moreover, this solver in Basilisk first advances the fluid properties to a mid-step $n+1/2$ which means that the density and viscosity are always lagging by half a step compared to the velocity/pressure field [37].

2.4.2 Surface tension

The surface tension term is given by $\gamma\kappa\delta_s\boldsymbol{n}$ where γ is the surface tension, κ is the curvature, n is the normal to the interface and δ_s is a Dirac function which expresses the fact that the surface-tension acts only on the interface [41]. This term is computed using the Continuum Surface-Force (CSF) approach introduced in [42]. To overcome its limitations, it is used alongside an accurate curvature estimate which uses a height-function technique [37].

2.4.3 VoF a front capturing method

To describe the interface of two immiscible fluids, Basilisk uses the volume-of-fluid (VoF). This method has been described in 1981 by Hirt and Nichols [43]. A volume fraction of the first fluid is introduced, $c(x,t)$. Where $c = 1$ we in are in the presence of fluid 1, where c=0 we have fluid 2 [37]. Each cell of the mesh has its c value. In the case of the cells that contain the interface between the two fluids, the density and viscosity are determined by linear interpolation

$$\begin{aligned} \rho(c) &= c\rho_1 + (1-c)\rho_2 \\ \mu(c) &= c\mu_1 + (1-c)\mu_2 \end{aligned} \tag{2.37}$$

An important advantage of the VoF over other interface tracing method is that the conservation of c ensures conservation of the volume of each fluid type in the system. The advection equation for the density can be replaced by the advection for the volume fraction, c:

$$\frac{\partial c}{\partial t} + \nabla \cdot (c\mathbf{u}) = 0 \tag{2.38}$$

where $c\mathbf{u}$ is the fraction flux area. The volume fraction is updated in time in two steps. First, the interface reconstruction step, in which the interface is approximated from the volume fraction field. Second, the fraction flux computation. In Fig. 2.7 we see a sketch of the reconstruction of the interface. On the left, we have the exact interface and on the right, we have the local linear interface. $\mathbf{m}$ is the normal to interface. Basilisk uses the Mixed Young Centered method to determine $\mathbf{m}$, this is an approach that combines two methods [44]. α is the intercept, which is uniquely determined by ensuring that the Volume-of-Fluid contained in the cell and lying below the plane is equal to c.

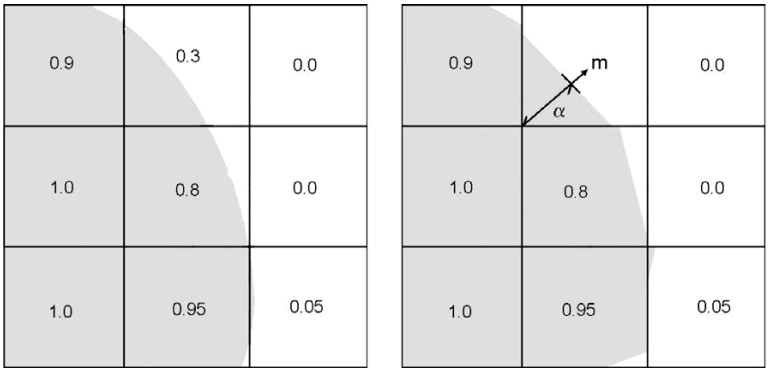

Figure 2.7: Sketch of the reconstruction of the interface. On the left is the exact interface and on the right is the linear reconstruction which maintains c. Figure from [45].

After the reconstruction step is complete, the volume fractions are updated in the advection step. In Fig. 2.8 we see a typical 2D advection problem. First, the fluxes in the x-direction are computed by multiplying the $\mathbf{u}$ components by the time interval Δt and then the y components are determined. We see that the fluid in the bottom right corner of the cell (i,j) has two possible directions, down or to the right. This illustrates the importance of reconstructing the cell after each sweep [46, 45].

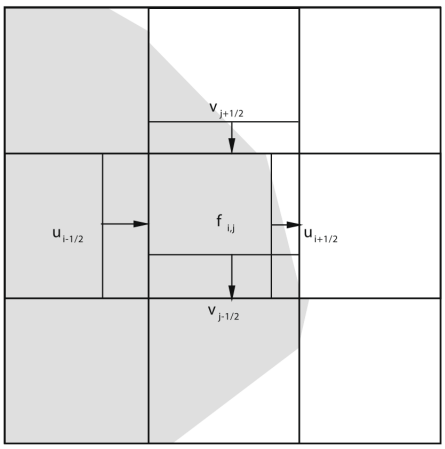

Figure 2.8: 2D diagram of a linear VoF surface reconstruction on a 3 × 3 block of cells with scaled velocity components. The fluid in each region goes to the neighboring cell. Figure from [45].

After the flux in all the dimensions has been determined the volume fraction is determined by Eq. (2.38) [46].

2.4.4 Adaptive mesh refinement

In 2D, Basilisk's domain is spatially divided into square finite volumes organised as a quadtree [41]. Each finite volume is named a cell. The length of the square is referred to as Δ. There are 4 types of cell, the root cell, which is the base of the tree. The parent cell, the direct ancestor of a cell, the children cell which are the descendent of a cell. Each parent has 4 children, in 2D. And the leaf cells, cells that do not have children. Each cell has a level. The parent cell is one level below its children cell, the root cell has level 0 and the leaf cell has the highest level [37]. In Fig. 2.9 we see an example of a mesh with cells up to level 4.

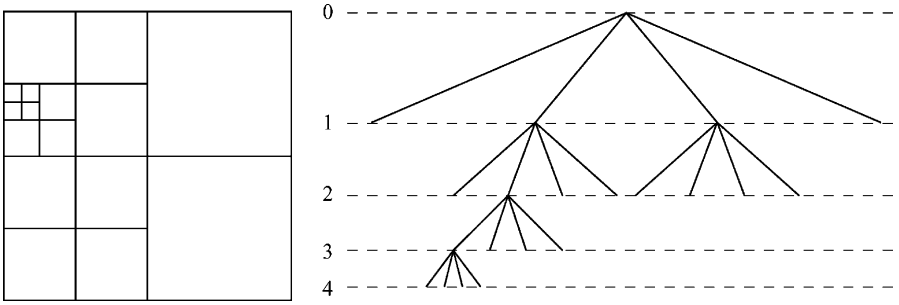

Figure 2.9: Sketch of a quadtree mesh and the corresponding tree. Figure from [47].

The grid in Basilisk is an adaptive mesh which greatly improves the simulation duration. An adaptive mesh is a mesh where the refinement depends on the spatial region. A threshold to the error of selected fields is set by the user. These are dimensionful parameters, they have the dimensions of the field they refer to. While the error of these two fields is not below the threshold the code will continue refining the grid in that specific part. In theory, any field can be given as the one on which the refinement depends on but it is good practice to use the primitive field, which in our case are the fraction field, which gives the interface, and the velocity field. Most of the users realize their importance and make use of these values, but there is another parameter that is also important to keep in mind, the variable TOLERANCE. This is a threshold for the Poisson equation since this one is also solved numerically. The tolerance is the maximum relative change in volume of a cell (due to the divergence of the flow) during one timestep, i.e., a non-dimensional quantity. Having slight changes will alter the results quite significantly, especially in cases where the density and viscosity ratios are high [48].

Chapter 3

Numerical methods and validation

To validate the capability of Basilisk to cope with capillary flow, we carry out two validations and compare the numerical results with theory from chapter 2 and reference data. First, in section 3.1 the results of droplet impact onto a pool are presented. In subsection 3.1.1 the numerical setup for this kind of impact is shown. In subsection 3.1.2 the temporal evolution of the cavity depth for different Weber numbers is evaluated and the maximum cavity depth dependence on Weber number is analyzed. Following this, in subsection 3.1.3, the crown width over time from Basilisk simulations is tracked and compared to experimental results. In the second part (section 3.2) the laser impact on a droplet is discussed. In subsection 3.2.1, the numerical setup of this phenomenon is presented and in subsection 3.2.2 Basilisk simulations of a laser impact onto a pool for different pressure profiles are compared to to the BI simulations from Ref. [13].

3.1 Droplet impact onto a pool

3.1.1 Numerical setup

In Fig. 3.1 the numerical setup is shown. Only half of the droplet is simulated, since we assume that the problem is axisymmetric. The simulation is done by using a mesh refinement of 11, which corresponds to 2048^2 cells. Consequently, $\Delta = 0.001D_0$, the initial droplet diameter is D_0=0.04 m, the initial distance to the liquid pool is $0.1D_0$, the domain length is $25D_0$, the pool height is $20D_0$ and the density and viscosity ratios are respectively $\rho_l/\rho_g = 1000$ and $\mu_l/\mu_g = 100$. The water properties are used: $\rho_l = 1000\text{kg/m}^3$, $\gamma = 71.3 \times 10^{-3}\text{N/m}$ and $\mu = 1 \times 10^{-3}$ Ns/m^2.

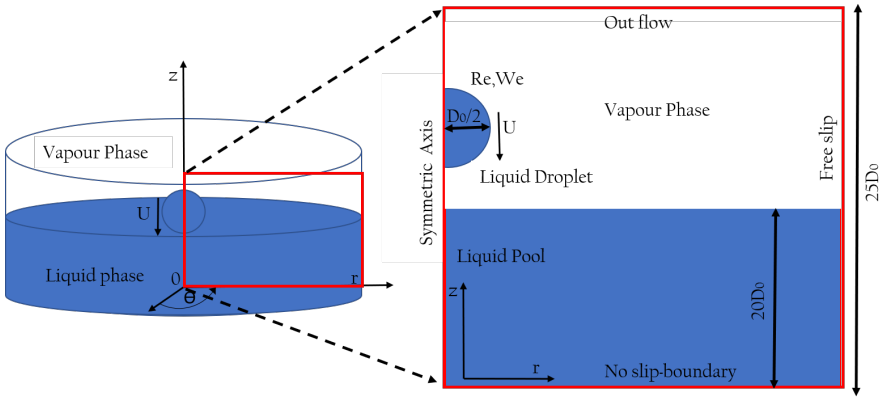

Figure 3.1: Computational setting for the droplet impact onto a liquid pool (a): The 3D perspective of the computational setting. (b): The cross section that we simulate. We use cylindrical coordinates. The droplet falls into the pool with a constant speed of U. The diameter of the droplet is $D_0 = 0.04$ m, the domain is $25D_0$. The pool height is $20D_0$. We apply an outflow boundary condition for the top, while the lateral walls are free-slip. As for the bottom of the pool, we apply a no-slip boundary. Figure from [31].

3.1.2 Cavity Depth for different Weber numbers

For the Cavity Depth study, we decided to use water's liquid properties and change the initial velocity. In

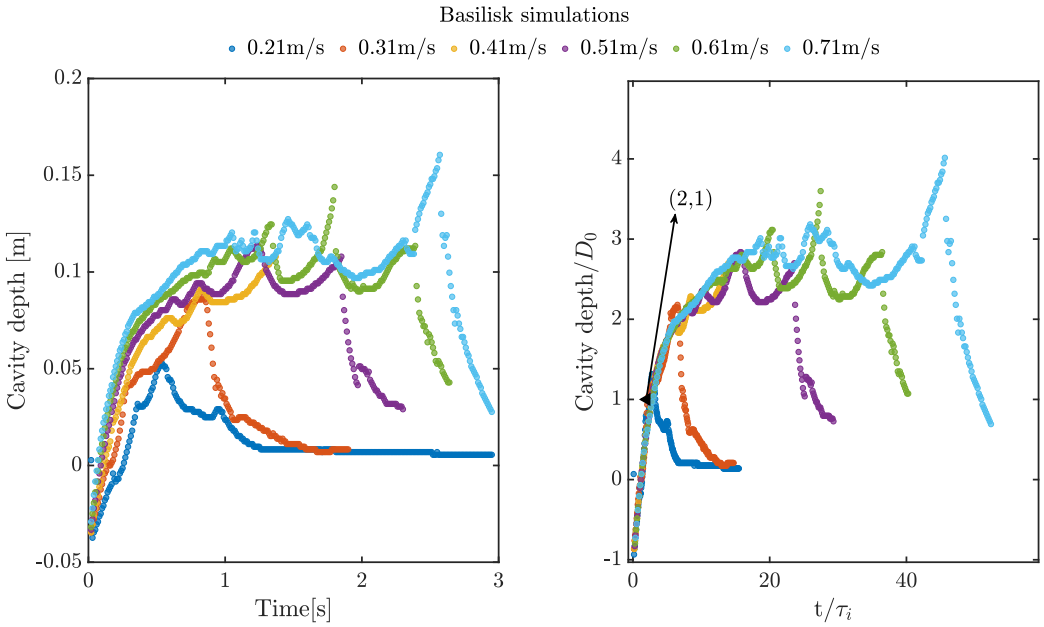

Figure 3.2: Cavity depth for the same liquid, different impact velocities, see legend. Different colors represent different impact velocities. On the left, dimensionfull axis are used. On the right, dimensionless axis are used which show the overlap of all the different cases up to approximately each curve's maximum cavity depth, before the surface tension overruns inertia. The point (2,1) is highlighted which is the theoretical penetration depth.

Fig. 3.2 we track the cavity depth over time for different initial velocities. On the left, we have in the y-axis the cavity depth in meters and the x-axis in seconds. On the right, we scale the cavity depth by the droplet diameter and the time by the inertial time, τ_i. We show the different cavity depths over time for different impact velocities (see legend) which translate into the following Weber numbers, We=[25, 54, 94, 146, 209, 283, 378]. We see that the cavity depth increases initially, showing a spike followed by a faster decrease. The curves present oscillations due to the travelling capillary waves. We can see that, as expected, when using dimensionless time, t/τ_i, all curves overlap up to when they reach the maximum cavity depth. We see that the curve goes through the theoretical point of (2,1), it takes $2\tau_i$ for the cavity to have the same depth as the initial droplet diameter, D_0 [25, 26, 27].

In Fig. 3.3 a double logarithmic plot of h_m/D_0 is shown as a function of Weber number. The maximum cavity depth, h_m, is taken as the maximum y value of each curve in figure 3.2. We observe a scaling of the h_m/D_0 in agreement with Eq. (2.5).

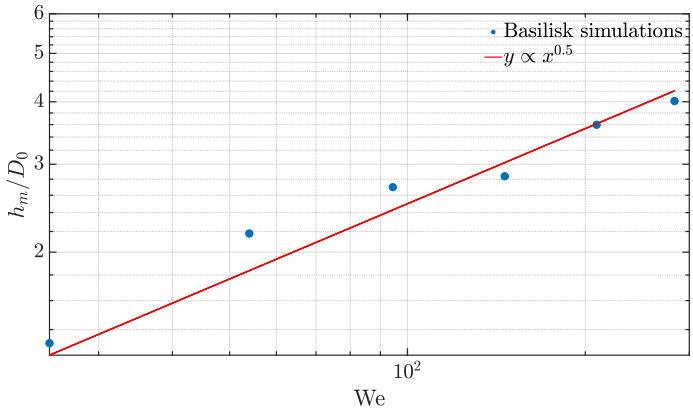

Figure 3.3: Double logarithmic plot of maximum cavity depth h_m divided by the diameter, D_0, as a function of Weber number. In red we see the scaling law given by Eq.(2.5). The Basilisk simulations show reasonable agreement with the scaling law.

3.1.3 Crown width

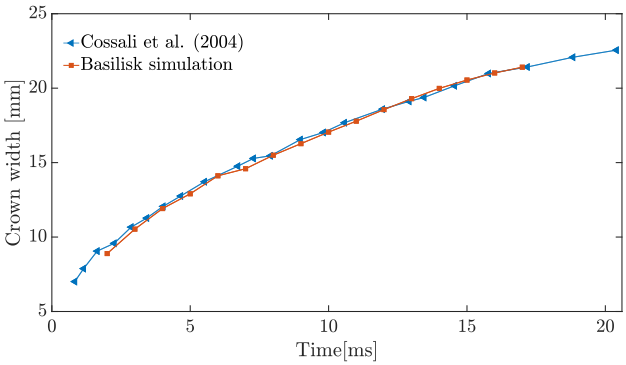

Figure 3.4: Crown width comparison between experiments from Ref. [49], in blue, and our Basilisk simulation, in red. Good agreement between the Basilisk simulations and the experimental data is observed.

In Fig. 3.4 we compare the simulation results with experimental data from Ref. [49]. The definition of crown width is shown in Fig. 2.2. We use the same values as in the experiments from Ref. [49].Thus, not only the the dimensionless numbers are the same but also the liquid and droplet properties. Simulation domain is $25D_0$, the initial droplet diameter is $D_0 = 3.82 \times 10^{-3}$m, the liquid density is ρ_l =998 kg/m^3 and liquid viscosity is $\mu_l = 1 \times 10^{-3}$kg/ms, the surface tension is $\gamma = 72 \times 10^{-3}$ N/m, the pool thickness is $0.6D_0$, and the density and viscosity ratios between the liquid and the gas phases are $\rho_l/\rho_g = 1000$ and $\mu_l/\mu_g = 100$, respectively. This results in We=667 and Re=13676. We show that the simulation agrees with experimental data.

3.2 Laser impact on a droplet

Basilisk has no predefined units, it will have the units that the user gives, for example, when defining the liquid properties. In the previous sections we set the liquid properties. However, this is not necessary. As explained before, in fluid dynamics, dimensionless numbers rule the behaviour. As long as the Weber number and the Reynolds numbers are the same we will observe the same phenomena.

3.2.1 Numerical setup

The main topic of this thesis is the simulation of laser impact on a droplet in Basilisk. In Fig. 3.5 we show the setup for the laser impact. This setup will be also used in chapter 4 and chapter 5. No-slip boundary conditions are applied on the top, lateral and bottom wall of the domain. As in Fig. 3.1 we use the cylindrical coordinate system and only simulate a cross-section, assuming symmetry around the z-axis. As in the droplet impact on a pool, to reduce the effect of the surrounding vapor we set the density and the viscosity ratio between the liquid and gas phase as ρ_l/ρ_g= 1000 and $\mu_l/\mu_g = 100$, respectively. The pressure profile is defined as coming from above. To set the droplet in motion, we introduce a velocity field where the fraction field is one, which corresponds to the liquid phase, see subsection 2.4.2. This velocity field is determined as described in chapter 2 with *Mathematica*. The Weber number, Reynolds number, U (the propulsion speed after the pressure profile is applied), D_0 are set and because the simulation need ones more variable, ρ is also defined. The Weber number is 790 and Reynolds is 1000, $D_0 = 2$, $\rho = 1000$. Consequently, $\gamma = 1.4$ and $\mu = 0.47$. These properties were determined for the case of We=80, Re=1000, D_0=2 and $U = 0.24$ and were carried out to all simulations. We can state that these variables are in SI units but they are arbitrary: we can change the liquid properties and as long as the dimensionless numbers are kept constant there is no difference.

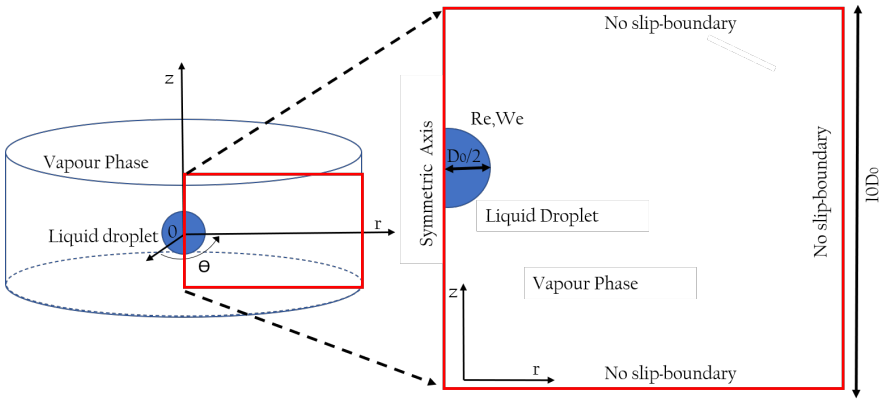

Figure 3.5: Computational setting of the droplet laser impact. (a) 3D setting of the computation domain, we use cylindrical coordinates, being z the axisymmetric axis. (b) show the cross section that we simulate. The pressure profile is applied from above and we use the no-slip boundary conditions. The domain is $10D_0$. We subtract the centre-of-mass velocity to simulate the behaviour in the co-moving frame. Figure adapted from [31].

3.2.2 Validation against Boundary Integral simulations

We start by comparing our Basilisk simulation results with previously Boundary Integral, BI, simulations done in Ref. [13]. This method does not solve the Navier-Stokes equation, but, instead it is based on the coupling of a Laplace equation for the flow potential to a lubrication approximation of the Stokes equation. This assumption excludes viscous effects [50, 51]. The lack of viscosity results in undamped surface waves that eventually result in artificial detachments of liquid from the edge. At early times, however, this artefact is not present [13]. In their work, the maximum height of the sheet h_m and its radius R (see Fig 3.6) are analysed [13]. Therefore, we track the same parameters for the Basilisk simulations.

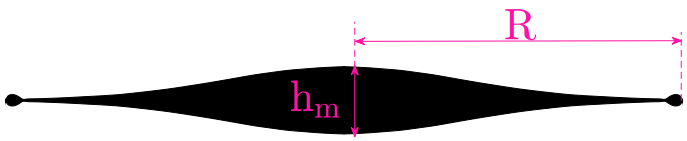

Figure 3.6: Simulation interface of the tin target after a some time has passed since the pressure profile was applied on the droplet. We see the sheet surrounded by the rim, the round edge blobs. Definition of maximum height, h_m, and radial length, R.

Fig. 3.7 shows the dimensionless radius and dimensionless thickness over dimensionless time for Basilisk simulations (full lines) and for the BI simulations (triangular markers). In our Basilisk simulations We=790 and D_0=2, so that R_0=1, since the pressure profile is given at dimensionless R_0=1. For our Basilisk simulations, we use a refinement of 2^{10} cells per dimension. As long as the non-dimensional parameters are the same, the physical phenomenon should be consistent, independently of specific fluid properties. The Reynolds number in all our Basilisk simulation cases is high enough to not affect our results. This also means that the absence of viscosity in the BI simulations from Ref. [13] should not case differences. Basilisk, as opposed to BI, solves the full Navier-Stokes equation and includes viscosity effects. Thus, in principle, Basilisk simulations are able to simulate the droplet time evolution up to times beyond what is possible in BI simulations. Nevertheless, even though these two type of simulations have a different approach, they show the same results for the early time droplet response. Their agreement gives us confidence in Basilisk.

We performed a convergence test by changing the liquid and gas phase's different density ratios and changing the Reynolds numbers between 500 and up to 3000. For the same dimensionless numbers We and Re, we tested different liquid properties and different centre of mass speeds. We also tested the TOLERANCE and the refinement level. There was a minimal discrepancy between all the simulations. The default value of TOLERANCE was used for the time period showed in Fig. 3.6. Reducing the variable TOLERANCE, showed no differences. However, higher Weber numbers and longer simulation periods, which lead to thinner sheets, refinement and TOLERANCE should be changed accordingly.

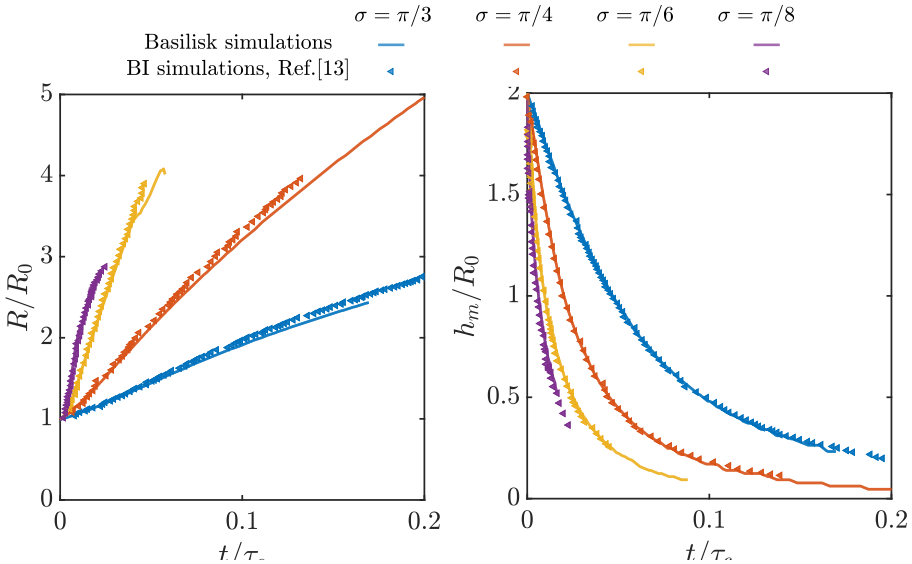

Figure 3.7: On the left panel the dimensionless radial length of the sheet, R/R_0, as a function of the dimensionless time, t/τ_c is plotted for different Gaussian pressure profiles and We=790. On the right panel, the time evolution of the maximum dimensionless thickness, h_m/R_0 is plotted for different Gaussian pressure profiles and We=790. The several Gaussian pressure profile differ in width, which is dependent on σ, see legend. We plot the results from Ref. [13], which were obtained by performing BI simulations and our results from Basilisk simulations. Good agreement between simulation codes is seen.

Chapter 4

Cosine Pressure Pulse onto a Droplet

In this chapter we will study the tin sheet's expansion trajectory, thickness, and mass distribution for a fixed cosine-shaped pressure profile given by $f(\theta) = \frac{3}{2\pi}\cos\theta H(\pi/2 - \theta)$ (see subsection 2.2.2), for various Weber numbers. The cosine-shaped pressure profile on the droplet surface is obtained from the projection of a uniform laser-beam profile. First, in section 4.2 we track the sheet radial expansion from the Basilisk simulations and compare it with the two models introduced in subsection 2.2.3 and with experimental data. Second, in section 4.3, we present the thickness profile and compare it to the available models. In section 4.3 we show a self-similar solution to describe the sheet thickness evolution. Lastly, in section 4.5 we compare the sheet and rim volume from the Basilisk simulations to experimental data. For clarity, every time we refer to Model we mean models that have been deduced in previous literature. When we mention simulations we refer to the work done in this thesis.

4.1 Numerical setup

The numerical setup is the same as shown in Fig. 3.5. The Weber numbers studied are We= [156, 320, 720] and the respective Reynolds numbers are Re=[1400, 2000, 3000]. The Weber numbers and their differences are set by the absolute propulsion speed, i.e. multiplying the velocity field by a constant. The centre-of-mass velocity used are U=[0.33, 0.48, 0.72]. The liquid properties, the ratio of the density between the fluid and the surrounding gas, and the size of the domain are the same as in subsection 3.1.3. We adapt the refinement to the Basilisk simulations case. For higher Weber numbers, which lead to thinner sheets, higher refinement is required. We implement an adaptive refinement mesh based on the fraction and velocity fields. We set a maximum refinement of 12, namely $2^{12} = 4096$ cells per dimension, for cases We=156 and We=320, and 2^{13}, for We=720. In this chapter we simulate the fluid response to a cosine shaped pressure profile. Considering that the velocity field induced by a cosine shaped pulse is mirror-symmetric around the horizontal plane, it results in a mirror-symmetric sheet around the horizontal plane, as presented in the next section. From Basilisk we extract the interface position over time. Since these are axisymmetric simulations, only the right half part of the droplet is simulated. We will show the left part for completeness, which is simply the mirror image of the right. From the interface we obtain the sheet radius, R, the thickness profile, h, and volume from the obtained contours.

4.2 Expansion dynamics

We start by qualitatively comparing the radial expansion for different Weber numbers followed by a quantitative analysis.

4.2.1 Qualitative comparison

Fig. 4.1 shows the time series of droplet contours from Basilisk simulations for three different Weber numbers when applying a cosine-shaped pressure on the droplet surface. The laser pulse is portrayed as coming from the top. The first row in Fig 4.1 presents the velocity fields for these three Weber numbers. Since the pressure profile shape is the same, at $t = 0$ the normalised velocity fields are identical. In this figure, contours in the same row have the same sheet radius, except for the last contour from the We=156 column. This case does not reach the large radius seen in the other two cases. The number on top of each contour represent the $t/$. The presented contours show an expansion that is mirror-symmetric around the horizontal

mid-plane, i.e. it has no curvature. We note that cases with a higher Weber number present faster radial expansion. Furthermore, we observe that at a given sheet radius, a higher Weber number leads to a smaller rim. We can further quantify the observations we made in terms of sheet radius, thickness, and rim and sheet volume. Among them, the sheet radius is determined by the distance from the sheet centre to its edge. The thickness is defined as the vertical difference between the upper and lower limit of the contour. The sheet volume is obtained by integrating the discretised volume element $2\pi r\delta rh$ from the sheet centre to the rim. In the following sections we will show the data of these parameters.

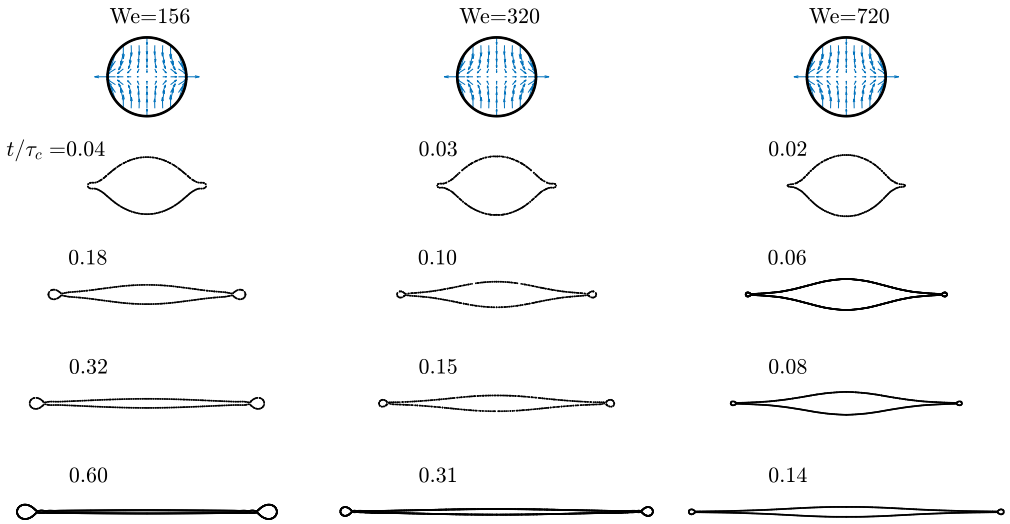

Figure 4.1: Droplet evolution obtained from Basilisk for a cosine shaped pressure pulse, and three Weber numbers We=156, We=320 and We=720. Respective Weber numbers are found at the top of each column. Each row has the same drop radius, except for the last row of the first column, where for this specific Weber number the maximum sheet radius is obtained. In the first row the velocity field at $t/\tau_c = 0$ in the comoving frame is shown. On the top of each contour we indicate the dimensionless time, t/τ_c. An increase of Weber number leads to a smaller rim for any given sheet radius and faster radial expansion.

4.2.2 Comparison with models

In Fig. 4.2 we find the dimensionless sheet radius evolution as a function of dimensionless time, t/τ_c, for the three Weber numbers also shown in Fig. 4.1. In both panels, the Basilisk simulations data is the same, only the models (from previous literature) differ, which is further explained below. We starting by noticing that the sheet radius expansion is characterised by two stages. First, the sheet expands, reaching its maximum, followed by the sheet's receding. Surface tension leads to continuously deceleration of the sheet up to the apex time, t_a. The apex time is the time when the velocity of the sheet expansion is zero. We note that the apex time is independent of the Weber number. Furthermore, we observe that higher Weber numbers lead to a more expanded sheet. In both panels, we plot experimental data from Ref.[52] for We=670±20 (the uncertainty is dominated by the uncertainty on the measurement of the droplet size, $D_0 = 30 \pm 1\mu$m). We see a reasonable agreement between the Basilisk simulation results when We=720, including the apex time. In the left panel, also Model 1 [Eq. (2.8)], from Ref. [29], and Model 2 [Eq. 2.22], from Ref. [13], for each Weber number are presented by the dotted line and the dashed line, respectively. Here, the centre-of-mass speed, U, is employed as an input to the Model 1 [Eq. (2.8)]; it is regarded as the characteristic speed. The values of U corresponding to We=156, We=320, We=720, are $U = 0.33$, $U = 0.48$ and $U = 0.72$ respectively. As for Model 2 [Eq. (2.22)], the energy partition $\frac{E_{k,d}}{E_{k,cm}}$ that is requested by the formula is set as 0.35, in line with Ref. [13]. As previously mentioned, the Basilisk simulations data in the right panel is the same as in the left panel. However, the model's data sets differ. In the right panel, we use u as free parameter for Model 1 and $\frac{E_{k,d}}{E_{k,cm}}$ as a free parameter for Model 2. This is explained further in chapter 6. To find the free parameter, we fit the Basilisk simulations data up to $0.38\tau_c$ to the models' equations. We choose to fit data to $0.38\tau_c$ this is the apex time of Model 1, which we see that does not agree with the simulation apex time. Only up to this time can the Basilisk simulation data and the Model 1 equation overlap. As a result, the values for u are 0.45,

0.68 and 1.07 for the Weber number of 156, 320 and 720, respectively. For $\frac{E_{k,d}}{E_{k,cm}}$ it was obtained 0.37, 0.40 and 0.43 for the Weber number of 156, 320 and 720, respectively.

It is shown in the right panel that both models differ from the sheet radius obtained from our Basilisk simulations. When using the characteristic speed in Model 1 and the energy partition in Model 2 as the fitting parameter we observe an overlap between the Basilisk simulations and Model 1 up to $t = 0.3\tau_c$, from then the equation from Model 1 underestimates the sheet radius. Model 2 still differs from the Basilisk simulations results. Regarding the apex times, both models' apex times differ from the Basilisk simulations one.

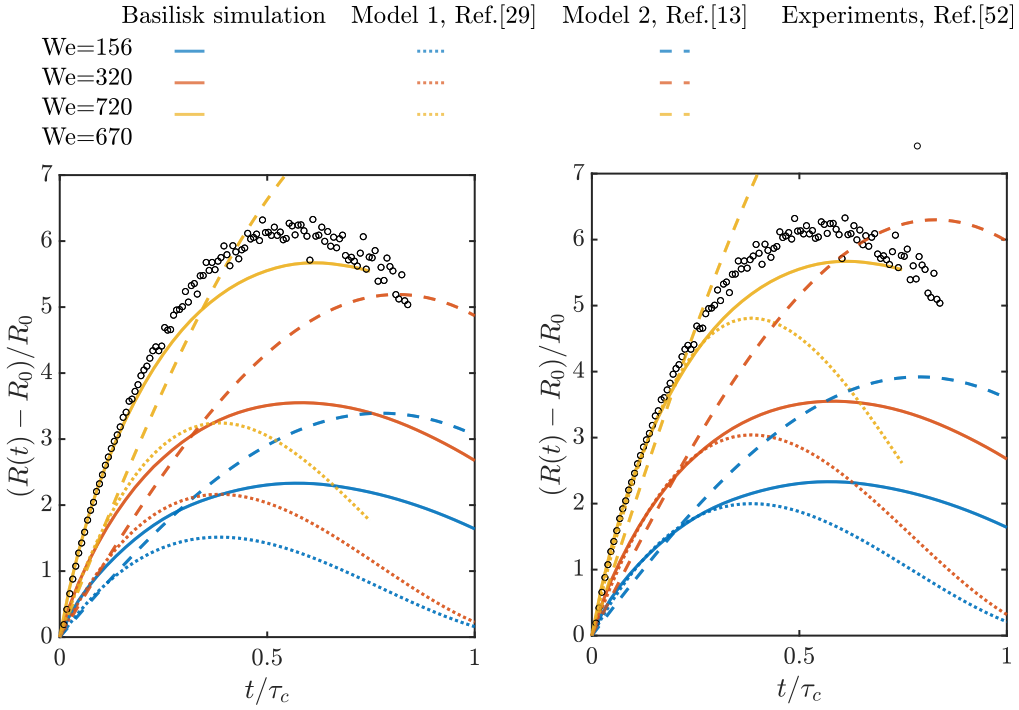

Figure 4.2: Dimensionless evolution of the sheet radius as a function of dimensionless time for three different Weber numbers, We=156, We=320 and We=720. The solid lines represent Basilisk simulation. The dotted lines represent Model 1 [Eq. (2.8)], and the dashed lines represent Model 2 [Eq. (2.22)]. Different colours represent different Weber numbers. In the left panel the centre-of-mass velocity is used to fill in 'u' in both models. In the right panel we treat 'u' and $\frac{E_{k,d}}{E_{k,cm}}$ as a free-fit parameter for Model 1 and Model 2, respectively. We fit Eq. (2.8) and Eq. (2.22) to the first part of the Basilisk simulations data, up to $t = 0.38\tau_c$. Experimental data with We=670±20, in empty black circles, is compared to the Basilisk simulation's We=720 case. The models differ from each other. The apex time of the sheet in the Basilisk simulations and in the model is independent of the Weber number but it is different in the three cases. The experimental data agrees with the radial expansion and apex time from the We=720 Basilisk simulation. Using u as free parameter leads to a good agreement between Model 1 and the radial expansion from the Basilisk simulations. Using $\frac{E_{k,d}}{E_{k,cm}}$ as a free-fit parameter brings Model 2 closer to the results of the Basilisk simulations but they still differ.

4.3 Thickness Profile

As mentioned in section 2.2, the models have assumptions, one of them is the sheet thickness. It is thus of particular importance to understand the true thickness profile. Figure 4.3 presents the scaled sheet thickness h/R_0 as a function of radial position r/R_0, for three Weber numbers, at the time delay of $t = 0.3\tau_c$. The thickness obtained from the Basilisk simulations is defined as the distance between the upper and lower boundary of the sheet contour, see example in the inset of Fig. 4.3. We analyse the thickness profile at $t = 0.3\tau_c$ due to the fact that the differences between the radial expansion models and radial expansion from the Basilisk simulation increase with time (Fig. 4.2). This is the latest time where there is still reasonable agreement between the Basilisk runs and the radial expansion of Models 1 and 2, see Fig. 4.2 panel (b). Furthermore, we choose the latest time where there is reasonable agreement because the curve from Liu *et al.* was obtained from data at $t \gg \tau_i$, where τ_i is the inertial time, see section 2.1, and in the Basilisk simulations $\tau_i = [0.1{-}0.2]\tau_c$.

Our Basilisk simulations indicate that for all Weber numbers, the sheet thickness decreases with the radial coordinate. Furthermore, when imposing a higher Weber number, the droplet deforms into a thinner profile, with larger sheet radius. As a result, more mass is retained in the sheet with the increasing of Weber number, and less mass will be in the bounding rim, see Fig. 4.3. Additionally, the sheet thickness of an expanding sheet from Models 1, 2 and Eq. (2.28) from Liu *et al.* [12] (see table 2.1) are plotted. As indicated by Eq. (2.8), the sheet thickness described by Model 1 requires the centre-of-mass speed, U, as an input parameter. Here, we use the value of u obtained from the fitting of Model 1 to the Basilisk simulations data as the input to Eq. (2.8), as it captures better the sheet's expansion dynamics, see Fig. 4.2 (b). Model 2, assumes a uniform sheet morphology. Such a thickness profile is thus illustrated as a horizontal dashed line in Fig. 4.3. The curve from Liu *et al.* is obtained by fitting an analytically derived solution [Eq. (2.12)] to the experimental data from laser impact onto a droplet, as described in section 2.3. This solution indicates a self-similar behavior of the sheet thickness evolution (see below). For this curve the centre of mass velocity, U, is used. Figure 4.3 indicates that, compared to the Basilisk simulation, Model 2 presents a considerable overestimation to the sheet thickness. This observation is expected, as Model 2 does not capture the rim dynamics and thus the mass accumulated in it. The sheet thickness from Model 1 is based on the thickness of a continuous jet impinging on a solid target [29]. Therefore, in Fig. 4.3, the inner central part of the sheet of Model 1 goes to infinity. As a result, the thickness from Model 1 shows better agreement with our Basilisk simulations in the outer part of the sheet. The curve from Liu *et al.* gives a reasonable estimation of the Basilisk results, for larger radial positions. It is important to mention that Model 1 and Model 3, on which the curve from Liu *et al.* is based on, give an expression for the sheet thickness. In these models the rim is acknowledged but they do not try to describe it.

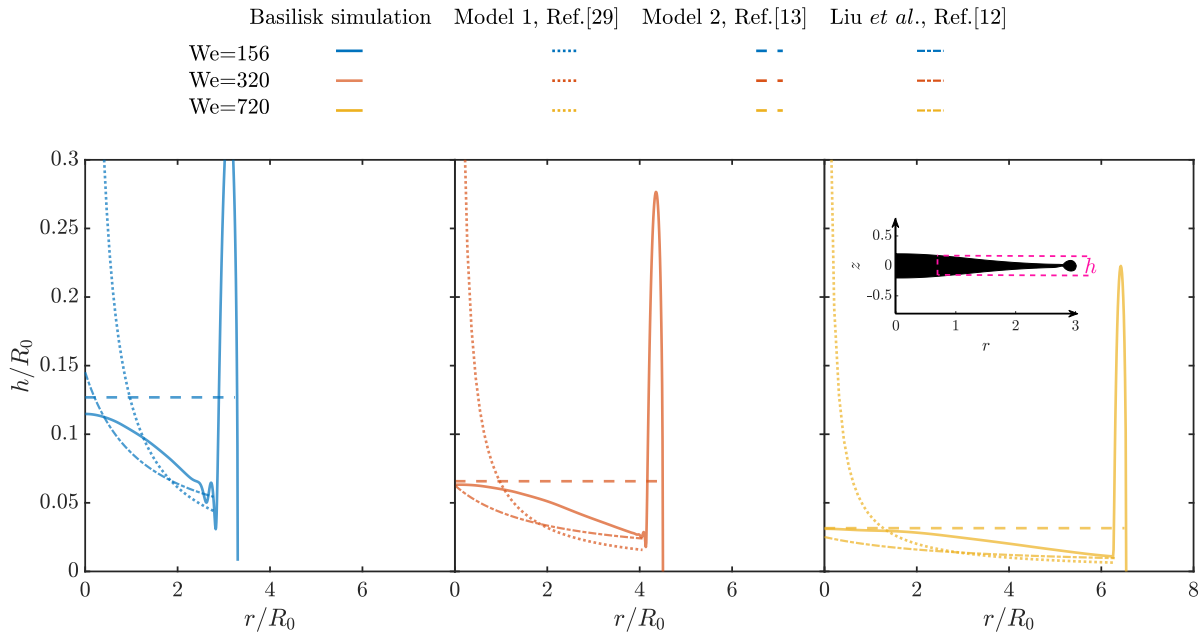

Figure 4.3: Thickness profile for different Weber number at the same time delay, $0.3\tau_c$, and three different models that predict the thickness. The same previous three Weber numbers are studied. Different colors represent different Weber numbers. The Basilisk simulations are represented by the solid lines while the different models are represented by the discontinued lines. The dotted line represents Model 1, the dashed line represents Model 2 and the dashed-dotted line represents the cruve from Liu et al.. For any given time, imposing a higher Weber number in the Basilisk simulations leads to a longer, thinner tin sheet and a smaller rim. All curves from previous literature differ from the results of Basilisk simulations. The curve from Liu et al. seems the closest one.

4.4 Self-similar solution of the sheet thickness

We see that the curve from Liu *et al.* does not fully capture the simulation results. However, this curve is obtained from fitting data to a reciprocal polynomial, found in Model 3 [32], which has free parameters. Therefore, we will check if our data can be described by the same reciprocal polynomial but with different coefficients. To determine the self-similar solution Ref. [32], assumes that is that the radial motion $v_r(r,t)$

dominates the velocity field and that $v_r = r/t$. Using our results from the Basilisk simulations we probe the temporal evolution of the radial velocity v_r at different positions of the sheet r and check if this assumption is valid in our simulations.

Figure 4.4 presents the scaled radial velocity v_r/r for the Weber number of 320 at z=0 and different radial positions as a function of time. The different colours represent the different radial positions, see the legend. Moreover, the assumption $v/r = 1/t$ is plotted as a black line. In this figure, for $t > 6$ ($t/\tau_c > 0.24$), we see a collapse of the Basilisk simulation results, meaning that the radial velocity increases linearly with the radial position, as suggested by Model 3. However, for earlier moments, an increasingly larger discrepancy is observed between $1/t$ curve and the results from the Basilisk simulation. Such a deviation is more pronounced when inspecting the velocity at the position closer to the sheet centre. Since that for larger radial positions, the data is closer to the velocity of Model 3, the sheet thickness of Model 3 is closer to the results from the Basilisk simulations for higher radial positions as shown in Fig. 5.4.

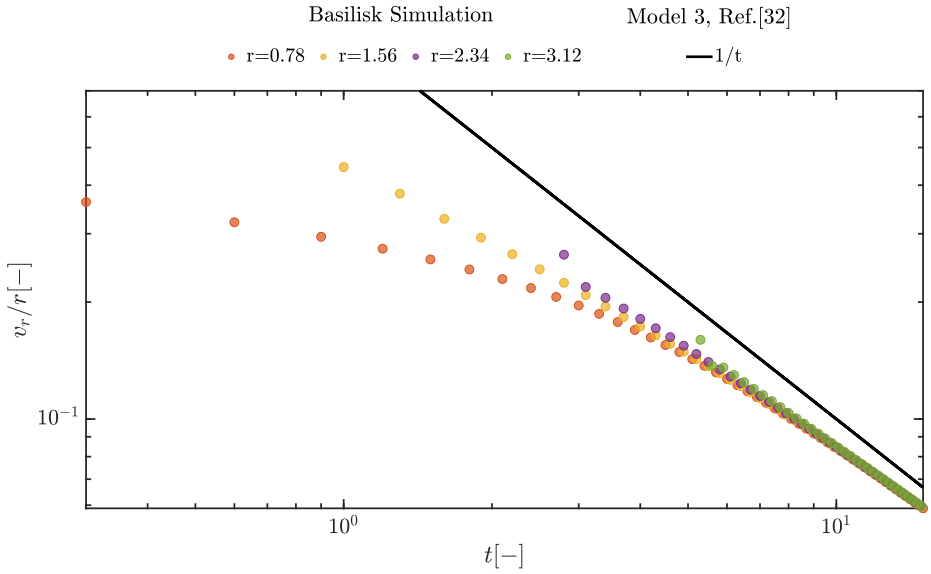

Figure 4.4: Radial velocity divided by radial position vs time for different radial positions in logarithmic scale. Different colored dots represent different radial positions from the Basilisk simulations. Black line is the equation 1/t. The inner radial coordinates do not overlap at early times. At late times the curves overlap and they follow the $1/t$ trend with a shift to the left.

Concluding that the radial velocity is close enough to the assumptions done by Model 3, we now will find the coefficients of Eq. (2.12) that best describe the sheet thickness obtained in our Basilisk simulations. In Fig. 4.5 we show the thickness profile for three Weber numbers at four different times. In the left panel, the thickness versus the radial position is shown. The right panel demonstrates the collapse upon use of the nondimensional similarity variables, h^*, r^* and t^*, see subsection 2.2.2. This is consistent with literature [32, 12]. The right-hand side panel shows that a very satisfactory overlap is obtained, independently of Weber number and time. Regarding the similarity profile F in 2.13, for our data set, we formulate it as:

$$F(x) = \frac{1}{a_2 x^2 + a_1 x + a_0}, \tag{4.1}$$

and we fit the obtained dimensionless data to this function. The coefficients obtained are: $a_0 = 4.2$, $a_1 = -8$, $a_2 = 21.7$. Comparing to the profile assumed in Ref. [32], Eq. (2.24), we do not include a_3 because we only evaluate at $t > \tau_i$ and a_3 is related to the early time dynamics. This means that this coefficient does not change our curve obtained at late time $t > \tau_i$. Instead, a_0 is introduced to account for the boundary condition at r=0.

In the right-hand side panel of Fig. 4.5, curves obtained from the laser droplet experiment, curve from Liu *et al.* [Eq.(2.27)], and from the droplet on a pillar, curve from Wang *et al.* [Eq. (2.25)], are shown. The

curve for the droplet laser experiments shown in this figure comes from Ref. [12]. This is the same curve as in Fig. 4.3 but in the self-similar variables. As stated before, the coefficients are: $a_0 = 1.65$, $a_1 = 6.93$, $a_2 = -2.48$. We see that these coefficients are different from the one from the Basilisk simulations. However, the similarity profile does not provide a fixed analytical expression, but instead, one that depends on the experimental conditions. In particular, it is believed to change with the laser focus to droplet diameter ratio. There is no conversion factor that allows for the translation from the pressure Gaussian shape used in the Basilisk simulations into the laser FWHM, the parameter measured in the experiments. This conversion factor is complicated to obtain because it is not the laser that directly sets the droplet into motion. Instead, it is the plasma created by the laser-droplet interaction that provides the momentum.

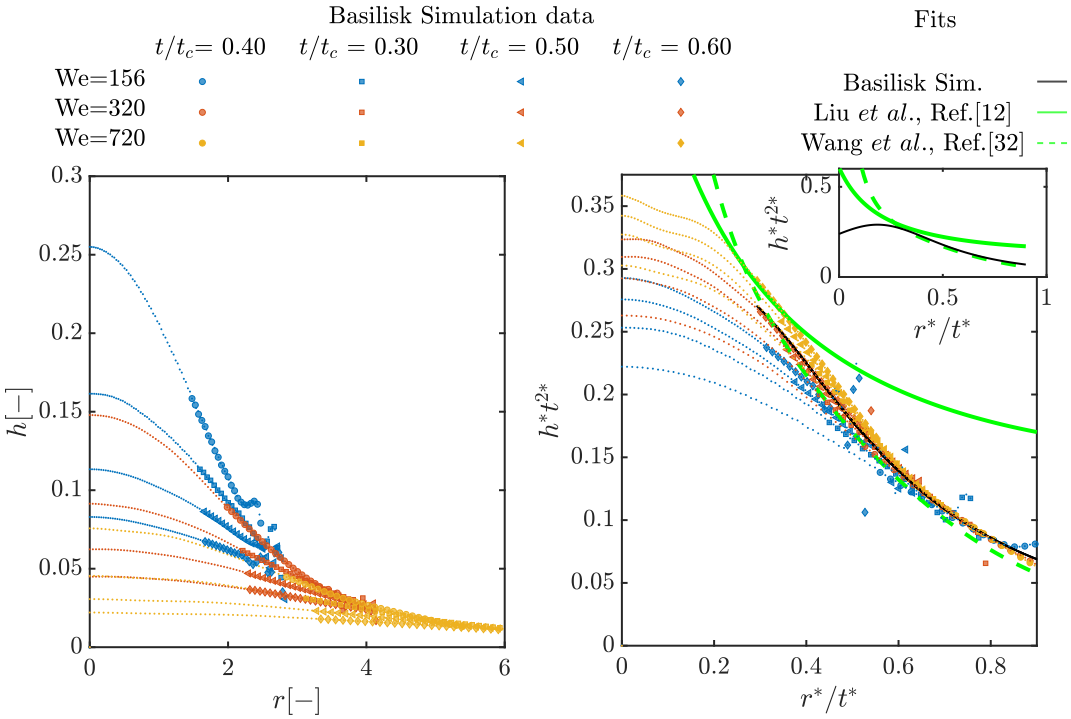

Figure 4.5: Thickness profile of the tin sheet versus radius. Various colors indicate various Weber numbers and different markers are different times, see legend. In the right panel we have dimensionless axes that allow for the finding of a single master curve. The solid black line represents the fit we find for the data set from our Basilisk simulations. The data presented by dots is not used for the fitting since it does not overlap. The solid green curve is the curve obtained in Ref. [12] when droplet-laser experimental data was fitted to the self-similar thickness profile solution, Eq. 2.27. We refer to it as the curve from Liu et al.. The dashed green curve represents the analytical expression obtained for droplet-pillar experiments with $\eta = 1.9$. This curve is found in Ref. [32]. We refer to it as the curve from Wang et al.. We see that when moving to the self-similar variables, for the outer part of the sheet, all thickness profiles fall into one single master curve. The Basilisk simulation fit agree with the curve from Wang et. al. and differs from the curve from Liu et al.. The inset shows an extrapolation of the fitted curve. When $r^*/t^* \to 0$, the curve from Liu et al. has a finite value but the curve from Wang et al. $\to \infty$. Furthermore we see that in the inner part of the sheet, the curve obtained from fitting data from the Basilisk simulations no longer agrees with the curve from Wang et al..

For the droplet-pillar experiments, curve from Wang *et al.*, in Ref. [32] different curves with different coefficients were obtained. These curves differ due to different droplet to pillar ratios, η. To choose which η is more appropriate we note that the cosine approximation of the pressure profile resembles a deformation by impact on a solid surface, this means $\eta \to \infty$. However, when using an infinitely large pillar, the viscous effects start being relevant. This is not seen in the Basilisk simulations. Being so, we opt for the highest η before the viscous effects become relevant, which is $\eta = 1.9$. As mentioned in subsection 2.2.2 in the case of a pillar, the similarity profile is given by 2.25. The similarity of the pillar droplet experiment and the dimensionless thickness profile from the Basilisk simulations is striking. However, for $r^*/t^* < 0.3$ the curvature of the two equations is different, which could be explained by the different physical origins of the droplet deformation and area of interest.

In Fig. 4.4 we see that radial positions further from the centre show better agreement with the velocity

assumption. Even though that at late times the inner radial positions show a good agreement, there is still a significant part of the time that does not agree with $v_r = r/t$. Therefore, in Fig. 4.5 we use only the furthest half of the thickness profile, $r > R/2$.

4.5 Volume ratio

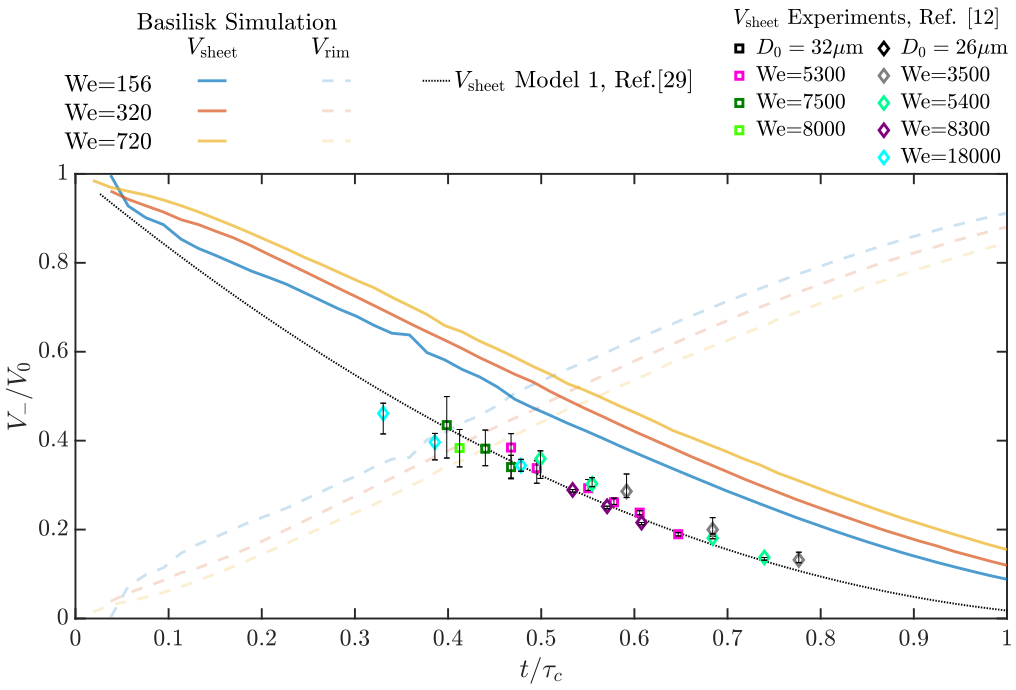

Figure 4.6: Volume ratio of the sheet and rim to that of the initial droplet V_0 as a function of the dimensionless time. Different colors represent the different Weber numbers. The dashed lines are the sheet volume and the full lines are the rim volume. The dotted black line is the model. Experimental data from Ref. [12] for two different droplet diameter and different Weber numbers are shown with the different markers and colours, see the legend. The volume in the sheet decreases over time for all different Basilisk simulations as well as in the experiments. The time evolution of the volume of Model 1 agrees with the experimental data. Both do not show a dependence on Weber number. However, Basilisk simulation show a dependence on Weber number. In Basilisk simulations where a higher Weber is imposed, more mass is retained in the sheet.

For the process of EUV light generation the distribution of the mass to be ablated is very relevant. Therefore, we must analyze the distribution of mass between the rim and the sheet. For a better understanding it is interesting to compare the sheet volume obtained in the Basilisk simulation to the sheet volume from Model 1. We compare only to this model because it is a more sophisticated model than Model 2, and Model 3 only characterizes the thickness, not the radial expansion. Moreover, the sheet volume from Model 1 has been previously compared to experimental data [12].

In Fig. 4.6, the volume ratio of the sheet and rim to the initial droplet volume is presented. There is no fragmentation in the Basilisk simulations so $V_{\text{rim}} = V_0 - V_{\text{sheet}}$. The various coloured lines represent the various Weber numbers. Considering that the Basilisk simulations is performed in an axisymmetric coordinate system, the sheet volume is obtained by integrating the discretised volume element $2\pi R\delta rh$ from the sheet centre to the rim. The square and diamonds markers are experimental data from Ref. [12]. Furthermore, the analytical expression of the sheet volume from Model 1 is presented by the black line in Fig.4.6. Model 1 assumes that $u_r = 0$ at the pillar edge. It is assumed that the sheet stays attached to the pillar while it expands. This means that the sheet within the pillar diameter is not taken into account.

Fig. 4.6 shows that for all Weber numbers, a larger fraction of the mass is retain in the sheet at early times. Considering that in Fig. 4.2 we see that sheet expands faster for higher Weber numbers, we conclude there is more mass retained in the sheet when the same sheet radius is reached. In addition, for higher Weber numbers,

despite leading to thinner sheets, more volume is retained in the sheet for any given time. Consequently, these cases have less mass in the rim. The sheet volume described in Model 1 [Eq. (2.10)] does not account for the mass at $r < R_0$. Experimentally, the thickness has been measured for different time scales and two different droplet diameters, which seem to follow the Model 1 prediction. As in the model, the inner thickness in the experiments is not determined. Despite this, we see that both the experiments and the Basilisk simulations indicate a high percentage of volume in the rim and the difference between the Basilisk simulations, model, and experiments is constant. However, the Basilisk simulations results have more mass than the model's prediction.

Chapter 5

Different Pressure profile onto a droplet

This chapter will explore the droplet's response to different pressure profiles at constant Weber number, We=320. We now use the Gaussian pressure profile introduced in subsection 2.2.3 given by $f(\theta) = c\exp\left[-\theta^2/\left(2\sigma^2\right)\right]$. We change the parameter σ which restrings the width of the pressure profile. The selected σ values are based on the division of π by an integer, as has been done in previous literature. The $\sigma = 0.73$ case is added to analyse literature statements. In section 5.2 the interface is shown, then the time evolution of the radial length is tracked and the radial expansion velocity is determined. In section section 5.3 the sheet's thickness profile is studied, and lastly, in section 5.4 we present the time evolution of the rim and sheet.

5.1 Numerical setup

The numerical setup in this section is the same as in chapter 4. The different cases have the same refinement of 12, except for the $\sigma = \pi/6$ case, which requires a more refined. We adapt it to the simulation time, increasing it from 12 to 14. The several normalized dimensionless pressure profiles used in this chapter are shown in Fig. 5.1. The cosine-shaped pressure profile is shown in blue and is the same one as in the previous chapter. We simulate different pressure widths by changing $\sigma = [\pi/3\ \pi/4\ 0.73\ \pi/3]$.

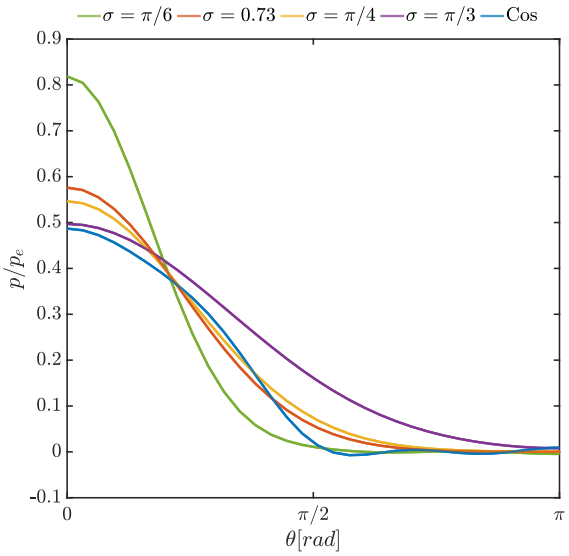

Figure 5.1: Pressure profiles as a function of the radial coordinate used in this section, see legend. The pressure scale p_e is obtained from the laser-pulse energy, details in Ref. [13]. Cos stands for the cosine-shaped pressure profile. The different σ values are the σ used in Eq. (2.20) to obtain Gaussian profiles with different widths.

5.2 Expansion dynamics

We start by qualitatively comparing the radial expansion for different pressure profiles followed by a quantitative analysis.

5.2.1 Qualitative comparison

In Fig. 5.2 we can see the time-lapse of the droplet contours for different pressure pulse with identical Weber numbers. These contours allow for a qualitative comparison. The pressure profile width decreases from left to right. We place the cosine case between $= 0.73$ and $= \pi/6$ since it has been previously stated that the cosine case showed the same energy partition as the $= 0.73$ case. As in Fig. 4.1 the interface is shown as if the laser comes from above and we see a cross-section of the droplet. The first row shows the different velocity fields imposed on the droplets. The contours at a given row have the same radius except for the last three rows of the first column. The $\sigma = \pi/4$ and $\sigma = 0.73$ cases are quite similar since $\pi/4 = 0.78$. Nevertheless, they still show differences. The first thing to catch our attention is the cosine column which stands out from all others. In the second row it already presents a rim, unlike others cases. The cosine case is also the only one that has mirror-symmetry around the horizontal plane. All other cases have a finite curvature, breaking this symmetry. This is expected as the velocity field imposed only shows this symmetry for the cosine case. The curvature becomes more pronounce for simulation where pressure with smaller widths are imposed. Regarding the sheet thickness profile we see that all cases present a thicker centre and thinner edges. This difference of the thickness with the radial position seems to increase for pressure profiles with a smaller width. In general, for cases where a pressure with larger σ is applied, the thickness is more uniform and the target presents a less pronounced curvature. Simulations where a pressure profiles with a smaller σ was applied show faster radial expansion and smaller rim.

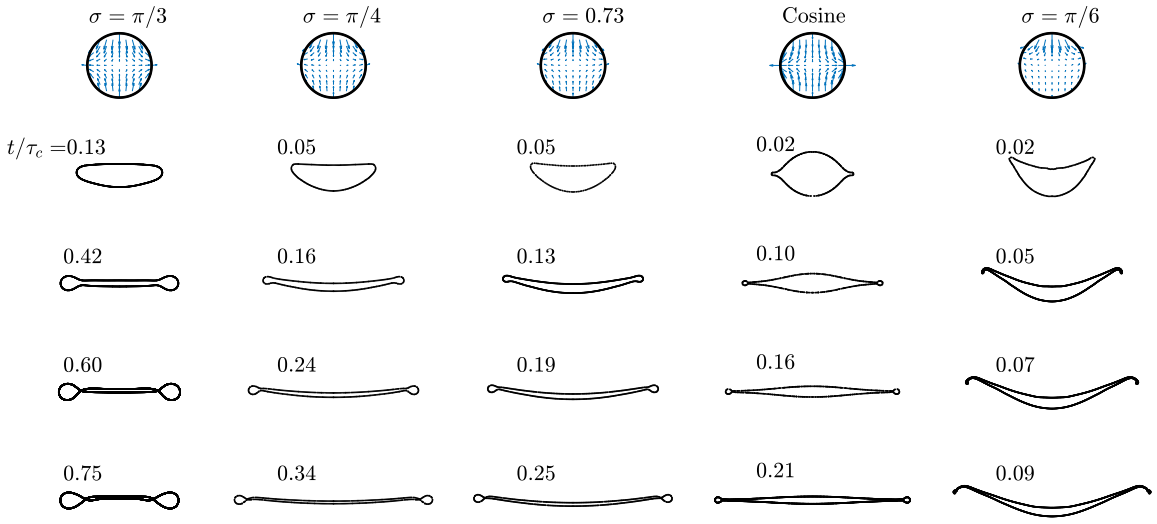

Figure 5.2: Droplet evolution obtained from Basilisk for We=320 and different pressure profiles. Cos stands for the cosine-shaped pressure profile. The different σ values are σ in Eq. (2.20) to obtain Gaussian profiles with different widths. Each column is a different Weber number and each row has the same drop radius, except for the last three rows of the first column. Respective σ values are found at the top of each column. In the first row the velocity field at $t/\tau_c = 0$ in the comoving frame is shown. The dimensionless time, t/τ_c in which each contour is sampled is indicated on top of it. Pressure profile width decreases from left to right. The sheet from the cosine Basilisk simulation is the only one that shows mirror-symmetry around the horizontal plane. Sheets from Basilisk simulations where a Gaussian pressure profile is imposed show curvature, breaking the mirror symmetry around the horizontal plane. A narrower pressure profile leads to more accentuated curvature of the sheet, smaller rim and faster radial expansion.

5.2.2 Quantitative comparison

The time evolution of sheet radius and its radial expansion velocity, $\dot{r}$ is presented. The top panel of Fig. 5.3 shows the dimensionless radius as a function of the dimensionless time. In the bottom panel, it is presented the scaled radial expansion velocities divided by the centre of mass velocities, $\dot{r}/U$, as a function of dimensionless time for the different pressure profiles. Various colours represent various pressure profiles. The Basilisk simulations are stopped once it is considered hat enough time has passed to grasp the behaviour, except for $\sigma = \pi/6$ case. This case is stopped due to the possible loss of simulation fidelity, see chapter 6. Moreover, we opt to show the most sophisticated model, Model 1 for comparison with chapter 4.

We observe in Fig. 5.2 that the maximum radius depends on the pressure profile. Cases where a smaller pressure profile width is imposed show a larger maximum radius and a faster expansion. Regarding the bottom panel, it is seen that in all cases, the radial expansion velocity first increases and then it decreases, except for the cosine and Model 1 cases. It is interesting to see that the narrower the pressure profile is, the higher is the $\dot{r}$ at a given time and the earliest its maximum is reached. The exception is the cosine profile which is explained by its different nature. The droplet exposed to the cosine shaped pressure pulse experiences its highest radial expansion velocity at $t/\tau_c = 0$, and decelerates from there on. The same is observed for Model 1.

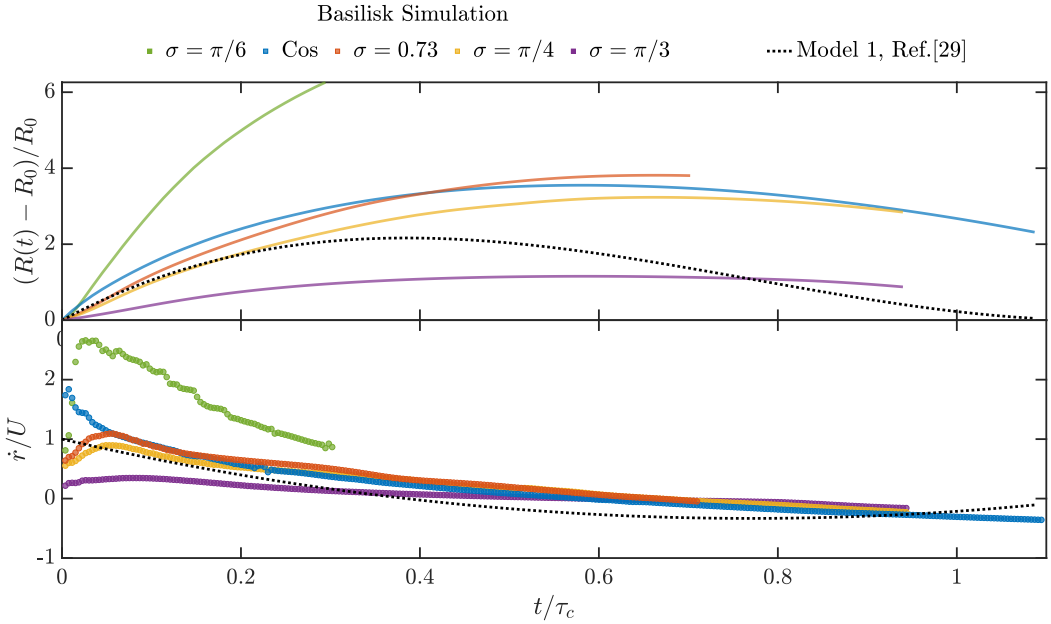

Figure 5.3: Time evolution of the radius and radial expansion velocity for different pressure profile, same Weber number, We=320. Different pressure profiles are shown with different colors. Cos stands for the cosine-shaped pressure profile. The different σ values are σ in Eq. (2.20) to obtain Gaussian profiles with different widths. For the $\sigma = \pi/6$ case the simulation is stopped earlier due to the computational time required and possible loss of simulation fidelity, this is discussed in chapter 6. The top panel shows that Basilisk simulations where a narrower Gaussian pressure profile is imposed lead to sheet with faster radial expansion and larger maximum radial length. Different widths of the pressure profile leads to a small different in the apex time of the sheets. The bottom panel shows that the sheets from simulations where a Gaussian pressure profile is imposed present an increase in radial expansion velocity followed by a decrease. When the cosine pressure profile is imposed, the radial expansion velocity of the sheet decreases with time. The $\dot{r}$ from Model 1 shows also a decrease over time.

5.3 Thickness profile

As in chapter 4, the thickness profile of the sheet is analysed. Fig. 5.4 shows the thickness profile for different pressure profile widths when the sheet has a radius of $4R_0$. The time at which this radial length from the top panel to the bottom one t/τ_c=[0.48, 0.33, 0.32, 0.11]. The $\sigma = \pi/3$ case is omitted as it does not reach this radius. We observe that to obtain a given radius, the wider the pressure profile is, the shorter

is the time delay. The thickness of the rim, at the edge of the sheet, decreases with σ, most significantly for $\sigma = \pi/6$. The sheet becomes more extended, so the rim shrinks in radial length and height. The thickness profile is also less uniform for narrower pressure profiles, showing an elevation in the droplet's centre. Even though the larger σ cases present a flatter sheet thickness, they still present a thicker centre than the edge of the sheet, as seen in this figure's inset.

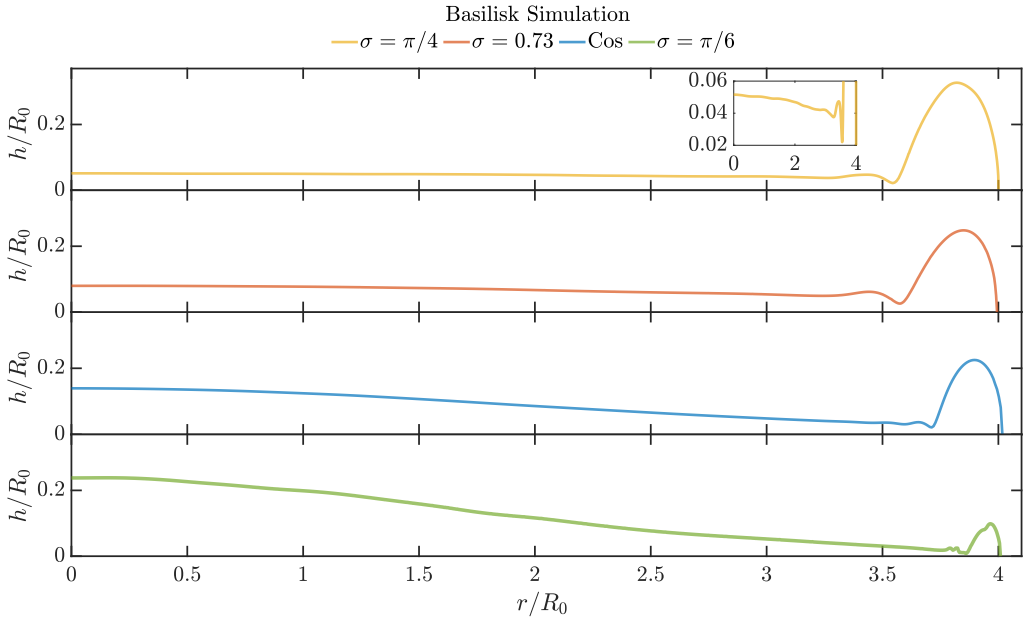

Figure 5.4: Thickness profile for different pressure profile widths, same Weber number, We=320 . Different pressure profiles are shown with different colors. Cos stands for the cosine-shaped pressure profile. The different σ values are σ used in Eq. (2.20) to obtain Gaussian profiles with different widths. Here the $\sigma = \pi/3$ case is omitted because it does not reach the dimensionless radius of $4R_0$. The rim is also shown. The dimensionless times at which this thickness profiles were observed are, from the top panel to the bottom one t/τ_c=[0.48, 0.33, 0.32, 0.11]. The inset shows the same as the top panel but with a smaller y-axis scale. Imposing a narrower pressure profile leads to sheets with a thickness profile less uniform and smaller rim.

5.4 Volume ratio

Fig. 5.5 presents the time evolution of the rim and sheet volume. Only 3 cases are presented to avoid overcrowding the graph. Since the $\sigma = \pi/3$ case is not as relevant as the others and the = 0.73 case is close to $\sigma = \pi/4$ case, these are removed. In the cosine case, the rim formation starts at an early time. For the Gaussian pressure profiles, this is not the case. Therefore, when we see a well-defined rim, it already has a significant mass, leading to a jump in the volume values. We see that the volume of the rim at a given time decreases with the decrease of the width of the pressure profile. From $t = 0.4\tau_c$ onward, the $\sigma = \pi/4$ case has a behaviour close to the Model 1 trend, as well as similar absolute values. Unlike the $\sigma = \pi/6$ case which has a behaviour similar to the cosine one.

In Fig. 5.6 the sheet volume as a function of the as a function of the instantaneous sheet radius $R(t)$ is presented for three pressure profiles. Time goes from top to bottom. For the cosine and the $\sigma = \pi/4$ cases, there are two possible values for the same radial length since the simulation results before and after the apex time are shown. This further highlights that the sheet's volume depends on the sheet's radial length and the pressure profile. For the $\sigma = \pi/6$ case, the sheet volume is significantly larger than for the other cases and decreases slower with the increase of the sheet radius.

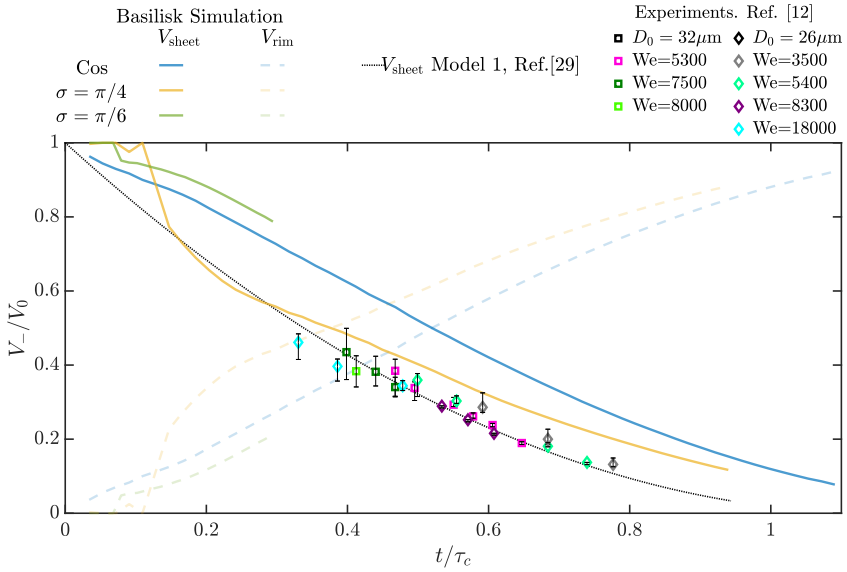

Figure 5.5: Time evolution of the relative volumes of rim and sheet for different pressure profiles, same Weber number, We=320. Different pressure profiles are shown with different colors. Cos stands for the cosine-shaped pressure profile. The different σ values are σ in Eq. (2.20) to obtain Gaussian profiles with different widths. The dashed lines represent the sheet; solid lines represent the rim volume. The black line represents Model 1 also shown in Fig. 4.6 for reference. The same experimental data as in in Fig. 4.6 is also shown, see legend. Independently of the pressure profile imposed in the Basilisk simulations, the mass retained in the sheet decreases with time. The time evolution differs depending on the pressure profiles imposed. Narrower pressure profiles lead to more mass being retained in the sheet.

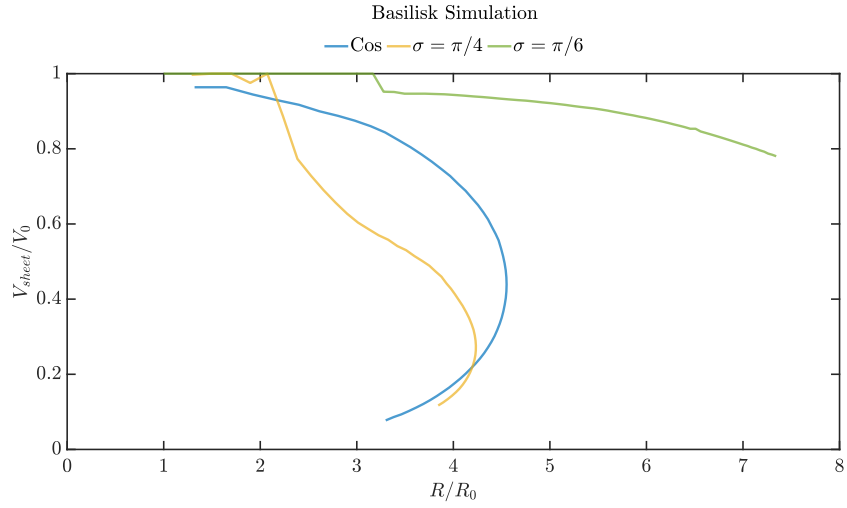

Figure 5.6: Relative sheet volume as a function of the sheet's radial length, R, for different pressure profiles, same Weber number, We=320. Different colors represent different pressure profiles. Cos stands for the cosine-shaped pressure profile. The different σ values are σ in Eq. (2.20) to obtain Gaussian profiles with different widths. Time goes from top to bottom. The mass in the sheet starts decreasing at different radius depending on the pressure profile applied on the droplet surface. The mass in the sheet for any given radius depends significantly on the pressure profile. When a narrower pressure profile is applied on the droplet surface, the mass retained in the sheet is larger.

Chapter 6

Summary and Discussion

In this chapter we summarise and discuss the results presented in chapters 4 and 5. In section 6.1 a summary and validation of Basilisk simulation is presented. In section 6.2 we report the new insights on the droplet expansion after applying a pressure profile. Finally in section 6.3 we comment on the optimum pressure pressure profile that minimizes the mass in the rim.

6.1 Basilisk validation against experiments and models

This project's research question is **"What is the time evolution of the mass distribution of a droplet after a laser impact?"**. To analyse the mass distribution of the deformed tin target we used Basilisk, an open-source package for Computation Fluid Dynamics (CFD). This package allowed us to simulate the two-phase Navier-Stokes equation. The interface of the tin target is captured by means of Volume-of-Fluid, VoF, coupled with the an adaptive Cartesian mesh. We used an axisymmetric geometry, simulating only half of the droplet. First, for the validation of the Basilisk code, simulations of a droplet impact onto a pool were performed. These simulations showed a good agreement with previous literature. As a last step for the validation of Basilisk, the droplet response to a pressure profile was simulated. A specific velocity field on the droplet was imposed as a boundary condition. The velocity field is a result of a Gaussian or a cosine-shaped pressure profile, following Ref. [13]. We tracked the maximum sheet thickness, h_m, and the radius of the tin sheet, R, over time. Our Basilisk simulations were compared to boundary integral (BI) simulations done in Ref. [13] and good agreement between the two types of simulations was found. After the code validation we performed two sets of simulations. In the first set of simulations we imposed a cosine-shaped pressure profile, and change the Weber number, see chapter 4. In the second set, we kept the Weber number constant at We=320 and changed the pressure profile. We used the cosine shaped pressure profile and several Gaussian pressure profiles,of various widths, see chapter 5.

Unlike in experiments of laser impact on a droplet [12, 14, 29, 36], Basilisk does not show fragmentation. However, we are still able to conclude that Basilisk is a suitable code to simulate the response of a liquid tin droplet to a pressure profile. To study the validity range of the Basilisk simulations, we recall the phenomena that lead to fragmentation. As stated in subsection 2.2.3 there are two types of fragmentation, hole nucleation in the sheet centre and neck region, and rim fragmentation. These effects are a result of thermal noise and corrugation due to the competition between surface tension and a fictitious force caused by the deceleration of the sheet. Thermal noise and corrugations are amplified due to instabilities. Considering that we conduct an axisymmetric simulation, the rim's thickness is constant around the z axis, which implies that corrugations in the periphery are not seen, see subsection 2.2.3. Unlike the experiments, in our Basilisk simulations, everything is smooth and homogeneous; there is no noise. Consequently, there is no hole nucleation. Therefore we have to investigate the range of validity of our Basilisk simulations. To do so, we first define the criterion that determines this range. For this, we follow Ref. [14] to estimate at what dimensionless time the different breakup phenomena occur.

We saw in subsection 4.2.2 that when the velocity u was treated as a free parameter, our Basilisk simulations have the same radial expansion as the one from Model 1, up to this model's apex time. We also notice that the breakup times calculated in Ref. [14] are derived from a slightly modified version of the radial expansion of Model 1. Considering this, we fit Eq. (2.8) to our Basilisk simulation data and find the free parameter u, as we did in the left panel of Fig. 4.1. The obtained u values can be used to determine the parameters on which the breakup times depend, $\mathrm{We_d}$ and $\widetilde{\mathrm{We}}$, where $\mathrm{We_d} = \frac{\rho u^2 R_0}{\sigma}/3 = \frac{u^2}{6U^2}\mathrm{We}$ and $\widetilde{\mathrm{We}} = \mathrm{We_d}\frac{E_{k,cm}}{E_{k,d}}$. We

take $\frac{E_{k,cm}}{E_{k,d}}$ from Ref. [13] for the difference pressure profiles. The times provided in Ref. [19] are t_s, the time at which the first hole in the sheet is observed over $r/R_0 < 0.5$ and t_l, the time at which the first ligaments are observed. According to Ref. [14], for $\mathrm{We_d}$ and $\widetilde{\mathrm{We}}$ in this work, we obtain the breakup times in Tab. 6.1.

Pressure profile	We	t_s/τ_c	t_l/τ_c
Cos	720	1.4	0.13
	320	3.5	0.19
	156	8.2	0.26
$\sigma = \pi/6$	320	2.5	0.12
σ =0.73		4.6	0.21
$\sigma = \pi/4$		5	0.24
$\sigma = \pi/3$		7.7	0.47

Table 6.1: Ligaments and sheet hole nucleation time, t_l and t_s, respectively, determined theoretically. In the Appendix we present a table with the intermediate steps, including $\mathrm{We_d}$ *and* $\widetilde{\mathrm{We}}$.

First, we will discuss the hole nucleation in the centre of the sheet. Tab. 6.1 shows that our Basilisk simulations, which at most are up to τ_c, stop before the hole nucleation happens: all sheet breakup times are after the apex time of the radial expansion from Model 1. After the apex time of Model 1, the Basilisk simulations no longer agree the model, presenting a more stretched sheet than predicted, as it can be seen in Figs. 4.2 and 5.3. Since Ref. [14] takes the radial expansion model as input to determine the breakup times we need an alternative way to determine them once the simulation no longer agrees with the model. In the same paper, it is observed that experimentally the sheet breakup occurs approximately when $R/R_0 \approx 6$. The only simulated cases that stretch beyond $6R_0$ are when We=720 and the cosine pressure pulse is used and for the case where $\sigma = \pi/6$ and We=320 (if our Basilisk simulations would agree the model they would exhibit a smaller maximum radius). Taking into consideration this threshold, our Basilisk simulations in the case We=720 (cosine) and $\sigma = \pi/6$ (We=320) would present hole nucleation at at $t/\tau_c \approx 0.4$ and $t/\tau_c \approx 0.2$, respectively. We note that the Weber numbers studied in this report are smaller than the relevant Weber numbers in the semiconductor industry and that $t_s \propto \mathrm{We}^{-1}$. Even though sheet breakup is not significant in most of our cases, in industry-like conditions it becomes a dominating event. For the tin case, Ref. [14] did not mention the time of destabilisation in the neck region. Therefore we cannot estimate a definite value. However, in Ref. [14], it is shown that the neck destabilisation for another fluid did not differ much from the sheet breakup time.

For the ligaments we see that they appear at early times, namely $0.2\tau_c$. The ligaments' dependence on Weber number is weaker than the t_s dependence, $t_l \propto \mathrm{We_d}^{-3/8}$. Since the ligaments appear on the edge of the rim we expect that there is an overestimation of the rim volume in the Basilisk simulations.

In conclusion, the rim's ligaments appear within the Basilisk simulation time. We assume that they do not interfere with the time evolution of the sheet, but we acknowledge that their absence in our Basilisk simulations leads to an overestimation of the rim volume. The sheet and neck breakup only appears at later times. Only for two cases is τ_l within the simulation time period, We=720 (cosine) and $\sigma = \pi/6$ (We=320). It is possible to conclude that the results of the Basilisk simulations are reliable for all cases with respect to fragmentation issues, except for the two mentioned, which, conservatively, are valid up to $t/\tau_c \approx 0.4$ and $t/\tau_c \approx 0.2$, respectively.

Having established the validity of our simulations, we recall that in chapters 4 and 5 several sheet's properties from the Basilisk simulations were tracked and compared to analytical or empirical models, shown in Tab. 2.1. We have seen that these models could not always accurately describe the simulation results. Therefore, it is possible to conclude that Basilisk offers an improved way to study and guide future experiments.

6.2 Insights in the droplet expansion dynamics and results interpretation

In this section we justify some of the choices taken in our work and discuss the most interesting facts found.

6.2.1 Velocity and energy partition as free parameters

We have used the velocity, u and the energy partition, $\frac{E_{k,d}}{E_{k,cm}}$ as free parameters to fit models to our data that, in principle, do not have free parameters. Therefore we need to justify this choice. The choice of inter-

preting u as a free parameters is motivated due to the difference in physics between our Basilisk simulations and Model 1, and because Model 1 assumes that $U = \dot{r_0}$, r_0 is the early time radial expansion velocity. This assumption is not always valid. Fig. 5.3 shows how $\dot{r}$ changes with time and pressure profile. Consequently, $\dot{r_0}$ depends on the pressure profile. In Fig. 4.2 (b), where u was treated as free-fit parameter, a good agreement (up to Model 1's apex time) between our Basilisk simulations results and Model 1 was found. This shows that Model 1 is insightful for the first part of the sheet expansion if the correct characteristic speed is used.

The energy partition, $\frac{E_{k,d}}{E_{k,cm}}$, value in Ref. [13] is determined by assuming that the droplet deforms into a disk-like shape, i.e. a shape with homogeneous thickness. However, we have shown that this is not the case. Therefore, we use $\frac{E_{k,d}}{E_{k,cm}}$ as free parameter. By doing so, the discrepancy between our Basilisk simulations and Model 2 for the initial phase of the droplet expansion decreases. Both $\dot{r_0}$ and $\frac{E_{k,d}}{E_{k,cm}}$ are of particular importance as they indicate the fraction of the kinetic energy that goes into deforming the droplet, the main goal of the prepulse laser.

6.2.2 Time evolution of the radial expansion velocity

The importance of the characteristic speed has been highlighted for Model 1 but in all three models presented in this thesis show a dependence on a characteristic speed. These are the propulsion speed U or the sheet's initial radial expansion speed, $\dot{r_0}$. The ratio of these two velocities is also of significant importance. It is a measure of the fraction of laser energy used to radially expand the droplet. The higher $\dot{r_0}/U$ is, the higher is the fraction of energy used to deform the droplet. However, defining $\dot{r_0}$ is non-trivial. Our results from Fig. 5.3 show that for Gaussian pressure profiles the radial expansion velocity presents a sharp increase followed by a decrease over time until it reaches zero. This has not been reported in literature before. We observe that both Model 1 and the Basilisk simulation when a cosine pressure profile is applied have an always decreasing $\dot{r}$. The behaviour of $\dot{r}$ from Model 1 indicates that this model may be insufficiently accurate. The observed time evolution for the radial expansion velocity calls for special care when determining $\dot{r_0}$ experimentally. In experiments where $\dot{r_0}$ is determined, it is usually taken as the slope of the first data points of the sheet radius as a function of time [13]. This approach is prone to several uncertainties. The temporal resolutions of the fast cameras in experiments limits the number of points per unit of time. Consequently, since we show that the increase and decrease of $\dot{r_0}$ happens in a short period, it might be overlooked.

6.2.3 Modelling of the apex time

In Fig 4.2 we see that the apex time observed in experiments is close to the apex time seen in our Basilisk simulation. Model 1 and Model 2 show a significantly discrepancy with the experimental results, including different apex times. We note that the apex time from Model 1 occurs at earlier times than all simulated cases while the apex time from Model 2 occurs at later times. Fig. 4.3 shows that the thickness profile from the Basilisk simulation differs from Model 1 and Model 2. This implies that the radial expansion from Model 1 and Model 2, which take the thickness profile as input, are different from the radial expansion observed in our Basilisk simulations. Model 1 assumes that the thickness profile has a $1/r$ dependence. This leads to smaller mass concentration in the edges and higher concentration in the middle of the droplet. Consequently, the inertia of the sheet is smaller in Model 1 than in our Basilisk simulations. Surface tension pulls the liquid back while inertia drives the liquid to expansion radially. Therefore, the larger the inertia is, the larger is the radial length achieved and the later is the apex time. The apex time is reached when surface tension starts dominating over inertia. On the other hand, Model 2 assumes a uniform thickness, which leads to a larger sheet thickness at larger radial coordinates and smaller mass in the centre of the droplet. This implies a larger inertia than in the Basilisk simulations, leading to a later apex time.

6.2.4 Differences between the thickness profile from the Basilisk simulations and the thickness profile curves obtained empirically

Model 3 provides a universal sheet thickness which coefficients must be determined by fitting the data to it. In Fig. 4.3 we show the curve obtained in Ref. [12] for data from laser impact on a droplet experiment, the curve from Liu *et al.*. Even though this is the curve which shows the best agreement with the thickness profile from the Basilisk simulations, it still differs significantly. However this does not mean that our simulations are not valid. The universal equation from Model 3 has free parameters which are obtained from fitting the

equation to data. The discrepancy seen between our Basilisk simulations and the curve from Liu *et al.* is an indication that the simulated pressure profile imposed in the simulation differs from the one in the experimental setup.

In Fig. 4.5, we see the collapse curve for data for in the pillar impact experiments from Ref. [32], for to the laser impact experiment, and for the Basilisk simulations. The pillar impact curve is referred to as the curve from Wang *et al.*. We see that the Basilisk collapse curve shows good agreement with the curve from Wang *et al.*. When $r^*/t^* < 0.3$ we do not see the collapse of our data from the Basilisk simulations (discussed in the following subsection), and the extrapolation of our collapse curve differs significantly from the curve from Wang *et al.*. This discrepancy can be explained by the different deformation types. Additionally, the curve from Wang *et al.* does not analyse the thickness in the centre, within the pillar diameter. However, the similarity between our simulation and the curve from Wang *et al.* confirms, once again, the similarity between droplet impact on a pillar and laser impact on a droplet .

6.2.5 Self-similar universal collapse only found in the outer part of the tin sheet

To obtain the general sheet thickness of Model 3, a radial velocity, $v_r = r/t$ is assumed. In Fig. 4.4 the radial velocity dependence on r and t is presented for one of our Basilisk simulations. We see that for early times v_r/r from our Basilisk simulations does not agree with the $1/t$ assumption. This is in agreement with Refs. [32, 12], where it is stated that a certain time is needed to establish the $1/t$ dependence. In addition, the non-overlap of the curves in this centre of the droplet at early times indicates that $v_r(r) = r$ is not seen in the Basilisk simulations. The difference in r dependence is justified by the fact that to arrive to the dependence on r, Ref. [32] assumes the sheet expansion to be a 1D problem. Consequently, the vertical velocity is neglected and the velocity is characterized solely by its radial component. However, at early times the centre of the droplet is too thick to disregard the z component of the velocity. Considering that, it is expected that in Fig. 4.4 the radial velocity of smaller radial positions do not overlap. On the other hand, at large enough radial positions where the sheet is thinner, the suggested dependence on r is observed. The non collapse of simulation data has been seen before. Ref. [53] looks into the self-similar solution for the droplet impact on a wall and arrives to a less satisfactory collapse than the ones in Refs. [32] and [12] and also than ours.

6.2.6 Time evolution of the sheet volume

For the first time ever, Weber number dependence of the sheet volume is shown. Contrary to the volume time evolution from Model 1 [Eq. (2.10)] and experiments of laser impact on a droplet [12], our Basilisk simulations show that the volume in the sheet depends on the Weber number. In particular, we find that targets with higher Weber numbers retain more mass in the sheet. To explain the difference between the Basilisk simulations and Model 1 one should notice that the volume calculation from Model 1 does not take into account the volume in the centre of the droplet. There are two reasons for this. Model 1 thickness profile is based on the thickness of a continuous jet impinging on a solid target. Therefore, the inner central part of the sheet of Model 1 goes to ∞, as seen in Fig. 4.3. Consequently, we can not use the thickness profile in the centre of the droplet to determine the volume in the mentioned region. Furthermore, Model 1 assumes that $v_r = 0$ at the pillar periphery, with the sheet attached to the pillar while it expands [29]. Experimentally, the sheet's centre mass is not measured. This leads to an unknown in the volume fraction. This unaccounted volume fraction in the middle has been been described as thicker disk [12].

For the first time ever, the volume for different pressure profiles is studied. In Fig. 5.5 we show that not only the volume at a given time is different for distinct pressure profiles, but it also has a different time dependence. We conclude that narrower pressure profiles lead to smaller rim volumes and a faster expansion, reducing the amount of mass lost to the outside of the sheet. Fig. 5.6 shows that, for any given sheet radius, changing the pressure profile width leads to significant differences in the rim volume. In Tab. 6.2 we see the volume fraction present in the sheet for $t/\tau_c = 0.5$. The difference of sheet volumes for the highest and the lowest Weber number is around 10 %-points, and Fig. 4.6 shows that this difference is constant over time. Tab. 6.2 shows us that at the half capillary time the difference between the cosine and the $\sigma = \pi/4$ case is 12 %-points, being higher and lower at other times. However, we see that all simulated cases present a high percentage of the mass flowing from the sheet to the rim, as in the experiments and in Model 1.

We	Cos	$\pi/4$
720	0.55	-
320	0.51	0.39
156	0.45	-

Table 6.2: Fraction of the volume in the sheet at $t/\tau_c = 0.5$ for different Basilisk simulations.

6.3 Comments on the optimum pressure profile

We have simulated the pressure profile on a droplet, not the laser itself. Therefore we must investigate the link between the laser and the pressure profile. In the experiments, the pressure profile is not directly set by the laser, but by the plasma that forms when the laser interacts with the tin. This pressure profile is not a perfect Gaussian. Instead, it wraps around the whole droplet [15]. It is important to mention that this effect is not accounted for in the Basilisk simulations. We observed that in our Basilisk simulations, $\dot{r}/U$ depends on σ, the pressure profile width. In experiments it has been seen that $\dot{r}/U$ depends on the laser focusing conditions, droplet diameter and laser energy. The lower the laser energy and/or laser beam spot size to droplet diameter ratio, FWHM/D_0, the more deformation we see, i.e. the larger $\dot{r}/U$ is. Therefore the conversion from σ to FWHM is non-trivial. Having established that the conversion from laser to pressure profile is complex we can nevertheless give an indication for the optimum pressure profile in the following paragraphs. We start by selecting the characteristics that we would like the tin target to obtain. In summary, we want a target shape which allows for maximum percentage on the tin mass to be ablated. For this, we consider the thickness and the radius of the sheet to be important. Furthermore, we want to minimize fragmentation, which we here equate to minimizing the mass contained in the rim.

One of the reasons to expand the initially spherical droplet is because it is too thick and the main laser can not ablate the whole mass. Using a prepulse laser, this droplet is radially stretched. However, a thicker part in the edges is formed, the rim. Considering that we want to prevent from becoming too thick and setting us back to the initial problem, we should choose a pressure profile that shows a small rim.

Another reason to modify the droplet's initial shape is to use the main pulse laser more efficiently. We do it by stretching the sheet over the laser size. We should opt for a highly energetic, focused prepulse laser to reach the desired sheet size with a smaller rim. When simulating higher Weber numbers we observe faster radial expansion, and consequently, the desired sheet size is reached earlier, when the sheet carries more tin. In turn, the focusing of the pulse results in smaller rims for the same radial expansion.

Regarding the fragmentation, in Ref. [36] it is shown that the rim keeps a local Bo number of Bo=1:

$$\mathrm{Bo} = \frac{\rho(-\ddot{R})b^2}{\sigma} \simeq 1, \tag{6.1}$$

where $\ddot{R}$ is the radial expansion acceleration, and b is the rim's vertical diameter. Equation 6.1 indicates a self-adjustment of the instantaneous rim mass. This adjustment relies on the process of destabilisation, i.e., the formation of fragments. In other words, there is a threshold to the rim mass which, when exceeded, triggers fragmentation.

Studies in Ref. [14] show that the fragmentation happens when $R/R_0 \simeq 6$ or $h/R_0 = 10^{-2}$ [14]. Thus, the sheet should not be overly stretched. We saw in chapters 4 and 5 that targets with higher Weber numbers and to which narrower pressure profiles were applied, exhibit a faster radial expansion and smaller volume in the rim. We conclude that to limit fragmentation the pressure profile should have a narrow width and should provide a high propulsion speed to the tin target. It would also be beneficial to use such a pulse and shoot the second, the main pulse laser, at early times.

In addition, we can establish the link between Weber number and laser energy. Refs. [15, 28] establish the relation between the centre-of-mass speed, U, and the laser energy. These studies found that $U \propto E_{od}^{0.6}$, in which E_{od} stands for energy on the droplet and is defined as a fraction of the laser pulse energy that sets the droplet into motion. Since the Weber number We=$\rho U^2 R_0/\sigma$, we conclude that We $\propto E_{od}^{1.2}$. This means that an increase of the Weber number in our Basilisk simulations, done by increasing U, can be associated with an increase of the laser pulse energy.

Chapter 7

Outlook

In this chapter, we go over three paths that this work can converge to. We start by the droplet impact and laser impact comparison. We then go into the coupling of a plasma code, RALEF, with Basilisk. And finally, we show a toy model to simulate the laser ablation onto a pool.

7.1 Droplet impact onto a pool and laser ablation of a pool comparison

Laser ablation of a tin pool has been studied as a way to understand how the liquid divertor in a fusion reactor would behave in case of an ELM, as stated in chapter 1, and as a possible design for the EUV source in the nanolithography industry [20]. Apart from the cited reference, no literature is found on this topic. A theoretical study of laser ablation splashing is non-trivial. Therefore, the dynamics of the crown formed during the laser ablation is compared to the one formed upon droplet impact on a pool [20]. However, there is no literature on droplet impact onto a pool with the same dimensionless numbers as the ones in the laser experiments. We here show a preliminary Basilisk simulation with the same parameters as one of the laser experiments. We compare a droplet impact with the characteristics as given in Tab. 7.2 to a laser impact with 10 mJ laser energy, a spot size of 66 μm and pulse length of 8 ns. After performing a Basilisk simulation with an initial perfect sphere the results seen differ from the experiments. The influence of the droplet shape has been studied in [54], and based on their findings we decided to slightly change the ratios of the droplet diameters. We used the cross section of an ellipse, Fig. 7.1. The characteristic length scale for the laser case is defined as the first observable crown width and the characteristic velocity scale as the first observable crown velocity [20]. The simulation was performed by using 2^{11} cell per dimensions, TOLERANCE=0.9e-5 and with a domain of $25D_0$ with the fluid properties given in Tab. 7.1 and impact parameters in Tab. 7.2.

$\rho\,(\mathrm{kg/m^3})$	$\mu(\mathrm{kg/m\cdot s})$	$\gamma(\mathrm{N/m})$
6.99×10^{3}	1.5×10^{-3}	5.75×10^{-1}

Table 7.1: Fluid properties of the simulation and the experiment [20].

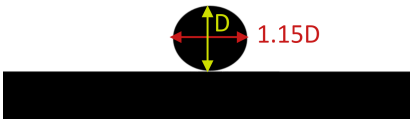

Figure 7.1: Simulation setup. The horizontal length of the ellipse is 1.15. The distance to the pool is $0.01D_0$.

Variables	Values
$D_{0_{D,L}}$(m)	2.5×10^{-4}
$U_{D,L}$(m/s)	28.0
τ_i(s)	1.2×10^{-5}
τ_c(s)	1.6×10^{-4}
Weber number	10^3
Bond number	10^{-3}
Reynolds number	10^4

Table 7.2: Impact parameters $D_{0_{D,L}}, U_{D,L}$, resulting timescales and dimensionless numbers of the studied splash. The inertial time τ_i, capillary time τ_c, and relevant dimensionless numbers are calculated using characteristic length scale $D_{0_{D,L}}$ and character characteristic velocity $U_{D,L}$. D_L and velocity U_L are chosen to be the first observable crown width and crown velocity, respectively. Table from Ref. [20].

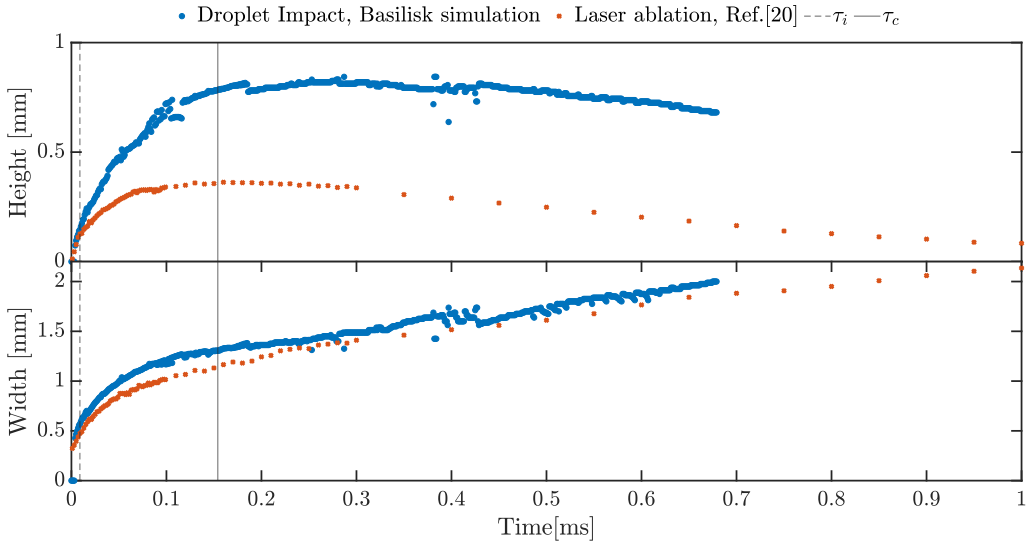

Figure 7.2: Height and width of the crown as a function over time for a droplet impact on a pool (Basilisk simulations), in blue, and laser ablation in a pool (experiments in Ref. [20]), in red. The inertial and capillary time as shown in dashes and full lines, respectively. The conditions are found in Fig. 7.1 and Tab. 7.2. For the crown width good agreement between the Basilisk simulation and the experiments is seen. For the crown height the simulation show a similar behaviour as the experiments but the absolute values are approximately double of the ones in the experiments.

In Fig. 7.2 we see the width and height of the crown for the droplet impact, from our Basilisk simulations and laser impact, from Ref. [20]. The width of the crown definition for the droplet impact is found in Fig. 2.2. The height is the vertical difference between the points where the crown is taken and the dashed line in Fig. 2.2 which represents the initial height of the pool. The crown width shows good agreement between the two phenomena. The height shows a similar behaviour but with approximately double the height, in case of the droplet impact. This first attempt shows the promising commutability of droplet impact and the laser ablation on a pool. To find the conversion factors from droplet to laser we propose a scan in the ellipse length scales, and its ratio as well as a scan in initial velocity.

7.2 RALEF

In this thesis, we used as input a pressure profile. In the experiments this pressure comes from the plasma which in turn is created due to the tin-laser interaction. This plasma wraps around the droplet and is not a perfect Gaussian. Therefore, it would be more accurate to simulate the plasma itself. Basilisk does not have the capabilities to do so. However, RALEF has. RALEF is a code where the 2D hydrodynamics equations are solved numerically alongside the equation of spectral radiation transfer [55]. 2D-RALEF has previously been used to simulate the tin-laser interaction of the EUV sources in the nanolithography industry [56, 57, 28]. RALEF uses the laser profile as an input and one of the outputs is the pressure profile. As mentioned in the introduction the plasma lifetime and the liquid response to the pressure exerted on the droplet by the plasma differ significantly. Consequently, we can separate the two phenomena. This allows for the coupling of RALEF and Basilisk. We can use the pressure output from RALEF as an input in Basilisk. In this section we present one case resulting from the coupling of the two codes. First, an expression for the pressure curve was determined by fitting Legendre polynomial to the pressure values from RALEF. Then the steps explained in chapter 2 can be taken to find the normalized pressure profile in such a way that the momentum in the laser direction is 1. We took these necessary steps and simulated in Basilisk a pressure profile from a 3 mJ laser with a focus of 115 μm focus on a droplet with a diameter of 50 μm from Ref. [28]. In order to facilitate the computational time and comparison between the Gaussian assumption and the RALEF pressure, the Weber number of RALEF pressure profile was reduced to 320. The same liquid properties as in chapter 4 and chapter 5 were and the resulting velocity field was multiplied by a constant smaller than one. The left panel from Fig. 7.3 shows the Gaussian pressure profiles with $\sigma = 0.73$ as shown in chapter 5 and the pressure profile from RALEF. We see it resembles the $\sigma = 0.73$ case. In the right panel of Fig. 7.3 we see the time-lapse of the sheet contours of $\sigma = 0.73$ and RALEF cases. We note that the curvature of the two simulations are different. This discrepancy can be explained by the difference of the pressure when $\theta = \pi$, where the Gaussian pressure profiles values are zero, unlike the RALEF pressure profile. We propose investigating the parameters studied in this work, time evolution of the radial expansion, thickness profile and time evolution of the sheet and rim volume, for different pressure profiles from RALEF. Not only should laser pulses with different focuses and energies be simulated but also different droplet diameters.

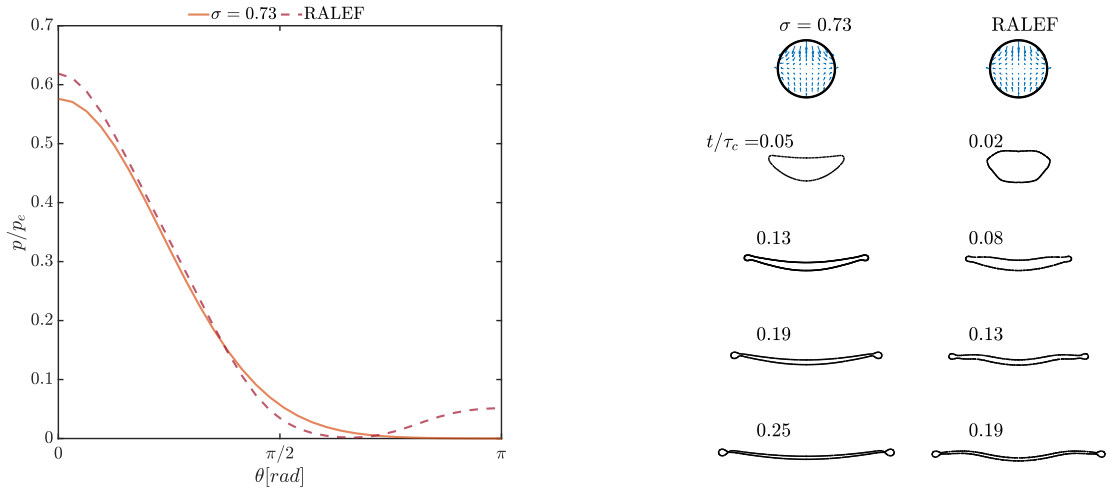

Figure 7.3: Comparison between a Gaussian pressure profile and a pressure profile resulting from the simulation of a laser on a droplet, by means of RALEF-2D. In the left panek Gaussian and pressure profiles with $\sigma = 0.73$ is represented by the solid line and the pressure profile from RALEF is represented by the dashed line. These pressure profiles were normalized in order for the axial momentum to be equal to one. The simulated case most similar to the RALEF is $\sigma = 0.73$, therefore we only show this one. In the right panel we show the time samples contours from Basilisk for comparison between the a Gaussian pressure profile and the pressure profile obtained from RALEF.

7.3 Toy model for a pressure profile on a pool

As mentioned, the laser ablation on pool has been considered as a good first approximation to study the liquid tin behaviour on a fusion reactor in the event of an ELM. Moreover it is proposed as an alternative EUV

source design for nanolitography applications. Simulating this phenomena, besides saving time and resources, it also gives access to information non accessible in experiments, e. g., cavity depth and pressure profile on the pool. Moreover, the simulation allows the study of a broader range of parameters. In Ref. [13] the limit when $\sigma \to 0$ is presented and the consequent velocity field is provided. We notice that in the limit when the size of the pressure pulse becomes negligible compared to the drop size, $\sigma \to 0$, the curvature of the droplet is not longer relevant, Fig. 7.4. The resulting velocity field is given by:

$$\begin{aligned} u_r(r,z) &= \frac{3rz}{2\pi\left(r^2+z^2\right)^{5/2}}, \\ u_z(r,z) &= -\frac{r^2-2z^2}{2\pi\left(r^2+z^2\right)^{5/2}}. \end{aligned} \tag{7.1}$$

When $r \to 0$ or $z \to 0$, u_r has a indefinite limit. Therefore, we impose directly in Basilisk that $u_r = 0$ when $r = 0$ or $z = 0$. When both $r \to 0$ and $z \to 0$, u_z has an indefinite limit, $u_z \to \infty$. Therefore we impose that when $r = 0$ and $z = 0$, $u_z = 100$. In Fig. 7.5 we show the early time velocity field and liquid response.

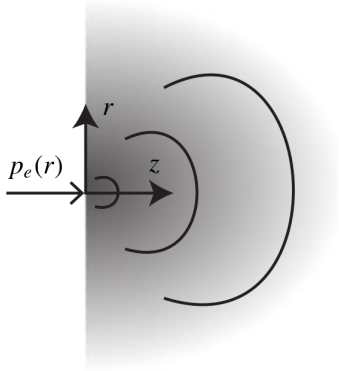

Figure 7.4: Pressure applied at the surface of an infinite half-circle with cylindrical coordinates r, z. Figure from Ref. [13].

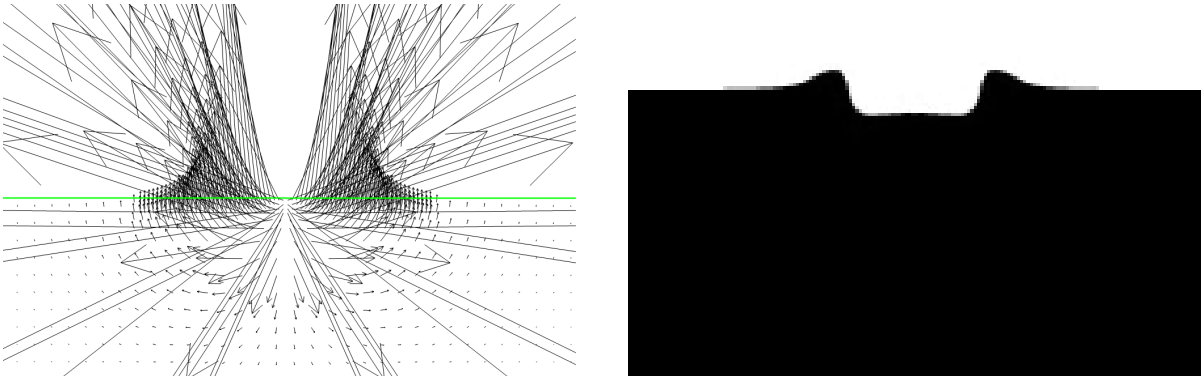

Figure 7.5: Pressure profile on a pool. In the left panel the initial velocity of the resulting velocity field on a pool at $t = 0$ is shown. In the right panel the interface of the liquid at shortly after the velocity field is applied is presented.

Further investigation is required of these velocity field application by performing more Basilisk simulations, for example, with different $u_z(0,0)$, and track the relevant parameters. Moreover, since we have shown that the coupling of RALEF and Basilisk is possible it could be beneficial to simulate the pressure profile from the laser on the pool and use it as input in Basilisk.

7.4 Fusion application

The studies performed in this thesis open a new method to study the liquid divertor response to possible high heat and particle fluxes from transients. These transients depend on reactor and plasma parameters. However it is known that the deposition area and time are significantly bigger than in the nanolitography industry. The deposition area is in the order of cm and the time of ms [58, 6], while in nanolitography the droplet has a diameter in the order of μm and the time is in order of ns. However, as we stated, the dimensionless numbers are what determined the hydrodynamic response of the liquid. The important step taken in this thesis is that it is possible to simulate pressure fields on Basilisk and study a valid hydrodynamic response. ELMs studies have gone a far way but there is still no theoretical description of the pressure profile they exert on the divertor. Thus, it will take time until a study like the one for the laser impact on a droplet to take place. However, the coupling of Basilisk and RALEF has been demonstrated. In addition, an example of a applying a pressure profile in a pool has been performed. To study the nuclear fusion application it would be interesting to see the simulation in RALEF of heat fluxes conditions similar to the ones in fusion or use another code that has previously been used to simulate an ELM, like JOREK [59, 60, 61]. However, we need to be aware of the timescales of the the plasma duration and the fluid dynamic times, which in the fusion case are closer together. This might compromise the coupling of two different codes. Moreover, we need to consider that in a fusion reactor the liquid metal will be subject to the forces due to the surrounding magnetic field and the plasma current.

Chapter 8

Conclusion

A droplet response to a pressure pulse has been numerically studied. We studied the radial expansion, thickness profile and volume distribution. This work's goal is to provide further understanding on a liquid droplet response to a pressure pulse. This is relevant from a purely scientific perspective but it is also important for industry applications. Laser-droplet interaction is used to create EUV light in the semiconductor industry. In this frame work, we want to retain more mass in the centre of the deformed target and minimize the expulsion of fragments.

Our first conclusion is that Basilisk is a valid new tool for the simulation of the pressure profiles on liquid targets. We use an axisymmetric simulation due to the reduced computational time in comparison with 3D simulations. In our Basilisk simulation fragmentation is not observed and according to Ref. [14] almost all simulated cases are within the range of validity, except for when We=720 and a cosine shaped pressure profile is applied and We=320 when a Gaussian pressure profile with $\sigma = \pi/6$ is used. We compared our Basilisk simulations results with models from previous literature and conclude that Basilisk simulations are an improvement compared to these models and to previously done simulations. This is mainly seen in the radial expansion time, in which the apex time from our Basilisk simulations agree with the one from experiments from Ref. [52], unlike the models. In addition, we provide a finite value for the thickness profile in the centre of the droplet, when $r \to 0$ and provide a clear rim profile. Moreover, compared to previous simulation methods, Basilisk provides the possibility to analyse the target parameters at later times. The possibility to simulate specific cases of Weber number, pressure profile shape and width, has already led to specific new insights into the droplet expansion dynamics. We highlight the radial expansion velocity which was demonstrated to change with the pressure profile and it shows a sharp increase over time followed by a slow decrease, unlike what has been documented so far. We also see a dependence of the sheet volume on Weber number and on pressure profile, which has not been reported before. Basilisk is now ready to take any pressure profile. The translation of the laser profile to a pressure profile for the Basilisk simulation input has yet to be found. If this conversation is available Basilisk is ready to implement it. Despite the missing laser to pressure profile translation, we already have suggestions on what is the best pressure profile to minimize the mass in the rim: a pressure profile which is narrow and also that leads the liquid target to have a high Weber number. Since high Weber numbers have been associate to lasers with high energy we can conclude that higher energy prepulse laser minimize the mass in the rim. In addition, we have shown that the coupling of RALEF and Basilisk is possible. This coupling provides a way to use the pressure profile from the laser-tin interaction as input to our Basilisk simulations. This means that in the future Basilisk can be used to find the optimal laser profile. Furthermore, Basilisk can be coupled with other codes to simulate fusion-relevant conditions.

Bibliography

[1] D. Maisonnier, I. Cook, P. Sardain, R. Andreani, L. Di Pace, R. Forrest, L. Giancarli, S. Hermsmeyer, P. Norajitra, N. Taylor, et al. A conceptual study of commercial fusion power plants. final report of the european fusion power plant conceptual study (ppcs). *EFDA report number EFDA (05)-27/4.10*, 2005. 1

[2] M. M. Waldrop. The chips are down for moore's law. *Nature News*, 530(7589):144, 2016. 1

[3] P. Rindt, T. W. Morgan, M. A. Jaworski, and N. J. Lopes Cardozo. Power handling limit of liquid lithium divertor targets. *Nuclear Fusion*, 58(10):104002, 2018. 1, 3

[4] D. Kurilovich. *Laser-induced dynamics of liquid tin microdroplets*. PhD thesis, Vrije Universiteit, 2019. 1, 2, 8

[5] P. Rindt. *The potential of liquid-metal 3D-printed heat shields for fusion reactors*. PhD thesis, Technische Universiteit Eindhoven, 2019. 1, 3

[6] A. Loarte, G. Saibene, R. Sartori, D. Campbell, M. Becoulet, L. Horton, T. Eich, A. Herrmann, G. Matthews, N. Asakura, et al. Characteristics of type i elm energy and particle losses in existing devices and their extrapolation to iter. *Plasma Physics and Controlled Fusion*, 45(9):1549, 2003. 1, 42

[7] A. Pirati, J. van Schoot, K. Troost, R. van Ballegoij, P. Krabbendam, J. Stoeldraijer, E. Loopstra, J. Benschop, J. Finders, H. Meiling, et al. The future of euv lithography: enabling moore's law in the next decade. In *Extreme Ultraviolet (EUV) Lithography VIII*, volume 10143, page 101430G. International Society for Optics and Photonics, 2017. 1

[8] T. Ito and S. Okazaki. Pushing the limits of lithography. *Nature*, 406(6799):1027–1031, 2000. 1

[9] C. Wagner and N. Harned. Lithography gets extreme. *Nature Photonics*, 4(1):24–26, 2010. 1

[10] V. Y. Banine, K. N. Koshelev, and G. H. P. M. Swinkels. Physical processes in euv sources for microlithography. *Journal of Physics D: Applied Physics*, 44(25):253001, 2011. 2

[11] S. A. Reijers. *Droplet impact phenomena in nanolithography*. PhD thesis, Technische Universiteit Eindhoven, 2019. 2

[12] B. Liu, D. Kurilovich, H. Gelderblom, and O. O. Versolato. Mass loss from a stretching semitransparent sheet of liquid tin. *Physical Review Applied*, 13(2):024035, 2020. 2, 7, 11, 23, 24, 25, 26, 33, 35, 36

[13] H. Gelderblom, H. Lhuissier, A. L. Klein, W. Bouwhuis, D. Lohse, E. Villermaux, and J. H. Snoeijer. Drop deformation by laser-pulse impact. *Journal of fluid mechanics*, 794:676–699, 2016. 2, 8, 9, 10, 11, 15, 18, 19, 21, 28, 33, 34, 35, 41

[14] A. L Klein, D. Kurilovich, H. Lhuissier, O. O. Versolato, D. Lohse, E. Villermaux, and H. Gelderblom. Drop fragmentation by laser-pulse impact. *Journal of Fluid Mechanics*, 893, 2020. 2, 7, 33, 34, 37, 43, 48, 49

[15] D. Kurilovich, A. L. Klein, F. Torretti, A. Lassise, R. Hoekstra, W. Ubachs, H. Gelderblom, and O. O. Versolato. Plasma propulsion of a metallic microdroplet and its deformation upon laser impact. *Physical review applied*, 6(1):014018, 2016. 2, 37

[16] J. P. H. E. Ongena and G. Van Oost. Energy for future centuries: will fusion be an inexhaustible, safe, and clean energy source? *Fusion science and technology*, 45(2T):3–14, 2004. 3

[17] R. Victoria Petrescu, R. Aversa, S. Kozaitis, A. Apicella, and F. I. Petrescu. Some basic reactions in nuclear fusion. *American Journal of Engineering and Applied Sciences*, 10(3), 2017. 3

[18] G. F. Nallo, G. Mazzitelli, L. Savoldi, F. Subba, and R. Zanino. Self-consistent modelling of a liquid metal box-type divertor with application to the divertor tokamak test facility: Li versus sn. *Nuclear Fusion*, 59(6):066020, 2019. 3

[19] A. L. Klein, W. Bouwhuis, C. W. Visser, H. Lhuissier, C. Sun, J.H Snoeijer, E. Villermaux, D. Lohse, and H. Gelderblom. Drop shaping by laser-pulse impact. *Physical review applied*, 3(4):044018, 2015. 4, 34

[20] J. Hermens, H. Gelderblom, B. Liu, J. Duffhues, P. Rindt, and O. O. Versolato. Laser-impact-induced splashing: An analysis of the splash crown evolution after nd:yag ns-pulse laser impact on a liquid tin pool. *Physical Review Applied*, 2020. 4, 38, 39

[21] A. L. Yarin. Drop impact dynamics: splashing, spreading, receding, bouncing.... *Annu. Rev. Fluid Mech.*, 38:159–192, 2006. 6

[22] S. Moghtadernejad, C. Lee, and M. Jadidi. An introduction of droplet impact dynamics to engineering students. *Fluids*, 5(3):107, 2020. 6

[23] R. Krechetnikov and G. M. Homsy. Crown-forming instability phenomena in the drop splash problem. *Journal of colloid and interface science*, 331(2):555–559, 2009. 6

[24] O. G. Engel. Crater depth in fluid impacts. *Journal of Applied Physics*, 37(4):1798–1808, 1966. 6

[25] E. Berberović, N. P. van Hinsberg, S. Jakirlić, I. V. Roisman, and C. Tropea. Drop impact onto a liquid layer of finite thickness: Dynamics of the cavity evolution. *Physical Review E*, 79(3):036306, 2009. 7, 16

[26] A. I. Fedorchenko and A-B. Wang. On some common features of drop impact on liquid surfaces. *Physics of Fluids*, 16(5):1349–1365, 2004. 7, 16

[27] A. Bisighini, G. E. Cossali, C. Tropea, and I. V. Roisman. Crater evolution after the impact of a drop onto a semi-infinite liquid target. *Physical Review E*, 82(3):036319, 2010. 7, 16

[28] D. Kurilovich, M. M. Basko, D. A Kim, F. Torretti, R. Schupp, J. C Visschers, J. Scheers, R. Hoekstra, W. Ubachs, and O. O. Versolato. Power-law scaling of plasma pressure on laser-ablated tin microdroplets. *Physics of Plasmas*, 25(1):012709, 2018. 7, 37, 40

[29] E. Villermaux and B. Bossa. Drop fragmentation on impact. *Journal of Fluid Mechanics*, 668:412, 2011. 7, 8, 11, 21, 23, 33, 36, 47

[30] C. Clanet and E. Villermaux. Life of a smooth liquid sheet. *Journal of fluid mechanics*, 462:307, 2002. 7

[31] B. Liu. Numerical simulation of oblique droplet impact onto a deep liquid pool. Master's thesis, Delft University of Technology, 2017. 8, 11, 15, 18

[32] Y. Wang and L. Bourouiba. Drop impact on small surfaces: thickness and velocity profiles of the expanding sheet in the air. *Journal of Fluid Mechanics*, 814:510, 2017. 8, 11, 23, 24, 25, 36

[33] O. O. Versolato. Physics of laser-driven tin plasma sources of euv radiation for nanolithography. *Plasma Sources Science and Technology*, 28(8):083001, 2019. 8

[34] R. Fabbro, J. Fournier, P. Ballard, D. Devaux, and J. Virmont. Physical study of laser-produced plasma in confined geometry. *Journal of applied physics*, 68(2):775–784, 1990. 8

[35] J. Eggers and E. Villermaux. Physics of liquid jets. *Reports on progress in physics*, 71(3):036601, 2008. 10

[36] Y. Wang, R. Dandekar, N. Bustos, S. Poulain, and L. Bourouiba. Universal rim thickness in unsteady sheet fragmentation. *Physical review letters*, 120(20):204503, 2018. 10, 33, 37

[37] S. Popinet. An accurate adaptive solver for surface-tension-driven interfacial flows. *Journal of Computational Physics*, 228(16):5838–5866, 2009. 12, 13, 14

[38] N. Djati. *Study of interface capturing methods for two-phase flows*. PhD thesis, Universite de Lyon, 2017. 12

[39] S. Popinet. Incompressible navier stokes solver. http://basilisk.fr/src/navier-stokes/centered.h#correction. 12

[40] C. Hirsch. *Numerical computation of internal and external flows: The fundamentals of computational fluid dynamics*. Elsevier, 2007. 12

[41] J. M. López-Herrera, A. M. Ganan-Calvo, S. Popinet, and M. A. Herrada. Electrokinetic effects in the breakup of electrified jets: A volume-of-fluid numerical study. *International Journal of Multiphase Flow*, 71:14–22, 2015. 12, 14

[42] J. U. Brackbill, D. B. Kothe, and C. Zemach. A continuum method for modeling surface tension. *Journal of computational physics*, 100(2):335–354, 1992. 12

[43] C. W. Hirt and B. D. Nichols. Volume of fluid (vof) method for the dynamics of free boundaries. *Journal of computational physics*, 39(1):201–225, 1981. 13

[44] S. Mirjalili, S. S. Jain, and M. Dodd. Interface-capturing methods for two-phase flows: An overview and recent developments. *Center for Turbulence Research Annual Research Briefs*, 2017:117–135, 2017. 13

[45] G. D. Weymouth and D. K-P Yue. Conservative volume-of-fluid method for free-surface simulations on cartesian-grids. *Journal of Computational Physics*, 229(8):2853–2865, 2010. 13, 14

[46] S. Popinet. Vof solver. "http://www.basilisk.fr/src/vof.h#lopez2015". 13, 14

[47] S. Popinet. Gerris: a tree-based adaptive solver for the incompressible euler equations in complex geometries. *Journal of Computational Physics*, 190(2):572–600, 2003. 14

[48] S. Popinet. Poisson solver. "http://basilisk.fr/src/poisson.h". 14

[49] G. E. Cossali, M. Marengo, A. Coghe, and S. Zhdanov. The role of time in single drop splash on thin film. *Experiments in Fluids*, 36(6):888–900, 2004. 17

[50] W. Bouwhuis. *Dynamics of deforming drops*. PhD thesis, 2015. 18

[51] R. Bergmann, D. Van Der Meer, S. Gekle, A. Van Der Bos, and D. Lohse. Controlled impact of a disk on a water surface: cavity dynamics. *arXiv preprint arXiv:0804.0748*, 2008. 18

[52] B. Liu. private communication, 2020. 21, 43

[53] J. Eggers, M. A. Fontelos, C. Josserand, and S. Zaleski. Drop dynamics after impact on a solid wall: theory and simulations. *Physics of fluids*, 22(6):062101, 2010. 36

[54] H. Shetabivash, F. Ommi, and G. Heidarinejad. Numerical analysis of droplet impact onto liquid film. *Physics of Fluids*, 26(1):012102, 2014. 38

[55] M.M. Basko, V.G. Novikov, and A.S. Grushin. On the structure of quasi-stationary laser ablation fronts in strongly radiating plasmas. *Physics of Plasmas*, 22(5):053111, 2015. 40

[56] M. M. Basko. On the maximum conversion efficiency into the 13.5-nm extreme ultraviolet emission under a steady-state laser ablation of tin microspheres. *Physics of Plasmas*, 23(8):083114, 2016. 40

[57] F. Torretti, J. Sheil, R. Schupp, M. M. Basko, M. Bayraktar, R. .A Meijer, S. Witte, W. Ubachs, R. Hoekstra, O. O. Versolato, et al. Prominent radiative contributions from multiply-excited states in laser-produced tin plasma for nanolithography. *Nature communications*, 11(1):1–8, 2020. 40

[58] G. De Temmerman, J. J. Zielinski, S. Van Diepen, L. Marot, and M. Price. Elm simulation experiments on pilot-psi using simultaneous high flux plasma and transient heat/particle source. *Nuclear Fusion*, 51(7):073008, 2011. 42

[59] S. Futatani, S. Pamela, L. Garzotti, G. T. A. Huijsmans, M. Hoelzl, D. Frigione, M. Lennholm, JET Contributors, JOREK Team, et al. Non-linear magnetohydrodynamic simulations of pellet triggered edge-localized modes in jet. *Nuclear Fusion*, 60(2):026003, 2019. 42

[60] A. Cathey, M. Hoelzl, K. Lackner, G. T. A. Huijsmans, M. G. Dunne, E. Wolfrum, S. J. P. Pamela, F. Orain, S. Günter, et al. Non-linear extended mhd simulations of type-i edge localised mode cycles in asdex upgrade and their underlying triggering mechanism. *Nuclear Fusion*, 60(12):124007, 2020. 42

[61] G. T. A. Huijsmans and A. Loarte. Non-linear mhd simulation of elm energy deposition. *Nuclear Fusion*, 53(12):123023, 2013. 42

Appendix A

Appendix

A.1 Adaptive mesh and velocity fields

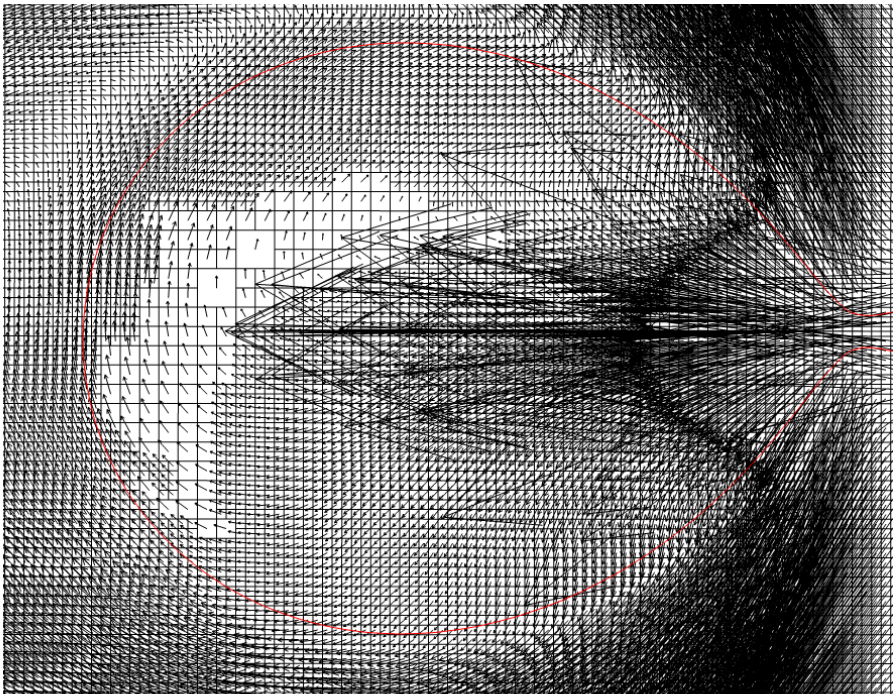

Figure A.1: Rim at t/τ_c=0.58 We=320. We can see the different mesh refinement and the velocity vectors.

In Fig. A.1 we can see the adaptive mesh refinement inside the rim and the velocity field vector. Further away from the interface and lower velocities the mesh is less refined. As the mass from the sheet's centre goes inside the rim it reduces its velocity by quite a significant factor. In ref. [29] it is discussed that if the size of the rim neck is much smaller than the rim itself, the velocity of the liquid in the rim should be much smaller. This is observed.

A.2 Volume calculation

In Fig. A.2 we show how we binned the data to determine the volume. This is an illustrative example, in reality we used more bins.

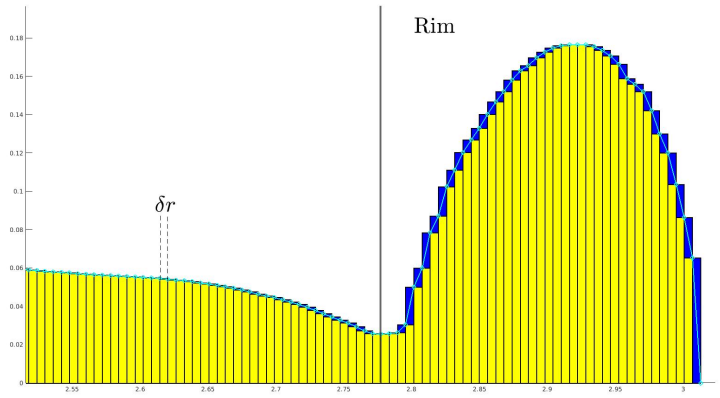

Figure A.2: Outer part of the sheet's thickness profile for We=320 and t=0.15τ_c. In Cyan is the thickness profile. In yellow the bin's lowest possible height and in blue the highest. Width of each bin is given by δr. On the right of the black line we count as Rim. Its start is defined as the smallest thickness.

A.3 Extra analysis for the fragmentation threshold

In Fig. A.3 we see the time evolution of the sheet thickness time evolution for the cases simulated. We see that only We=720 and $\sigma = \pi/6$ present a sheet thickness thinner that the threshold of $h/R_0 = 0.01$. Giving us further confidence in the simulation. It is interesting to note that the minimum sheet thickness continues decreasing over time, which means that for the same radial length the sheet thickness is not the same. This agrees with the late fragmentation seen in Ref. [14], where after the apex time, when the sheet is receding there is fragmentation. We notice also that it is always in the neck, once this is formed hat is the reason why we see a discontinuity.

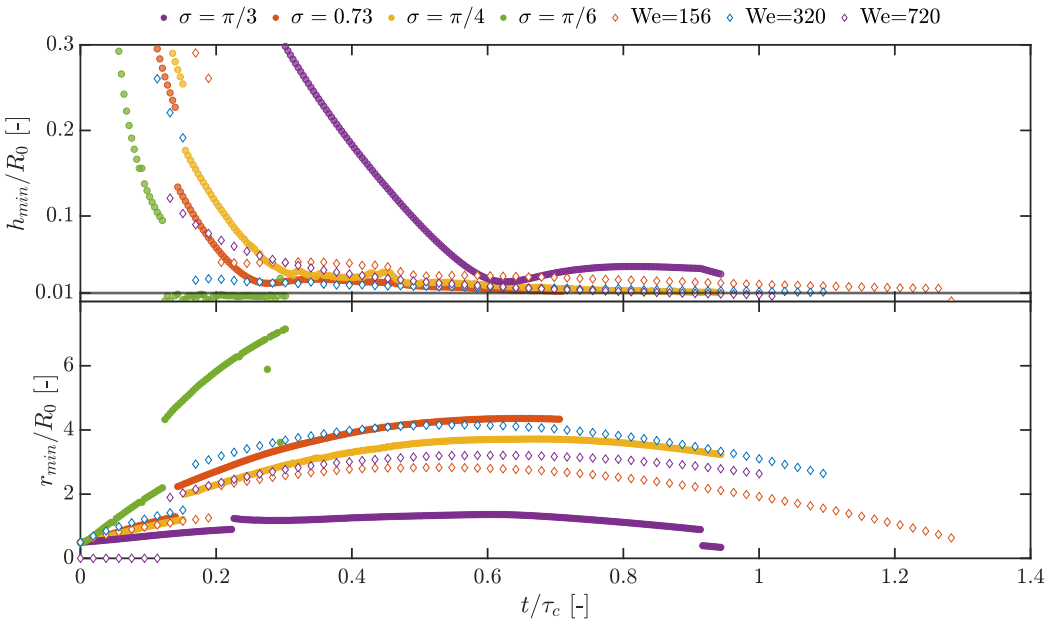

Figure A.3: Top panel minimum sheet thickness evolution over time for different cases simulated. The black solid line at 0.01 is the thickness at which rupture is seen. Bottom panel at which radial position this minimum thickness is found.

A.4 Detail on the determination of the breakup times

In Ref. [14] the Model on which the calculation of the breakup times is based on is given by:

$$\frac{R(t)-R_0}{R_0} = \sqrt{3\frac{E_{k,d}}{E_{k,cm}}\frac{\rho u^2 R_0}{\sigma}}\frac{t}{\tau_c}\left(1-\frac{\sqrt{3}}{2}\frac{t}{\tau_c}\right)^2. \tag{A.1}$$

The difference between this model and Model 1 the factor inside the square root. In Model 1 "$3\frac{E_{k,d}}{E_{k,cm}}$" is omitted. We fit our data to this equation, taking u as a free parameter, see Fig. A.4. In this figure we see that the model describes the Basilisk simulation when the cosine pressure profiled was used better than the simulations where Gaussian pressure profiles were imposed.

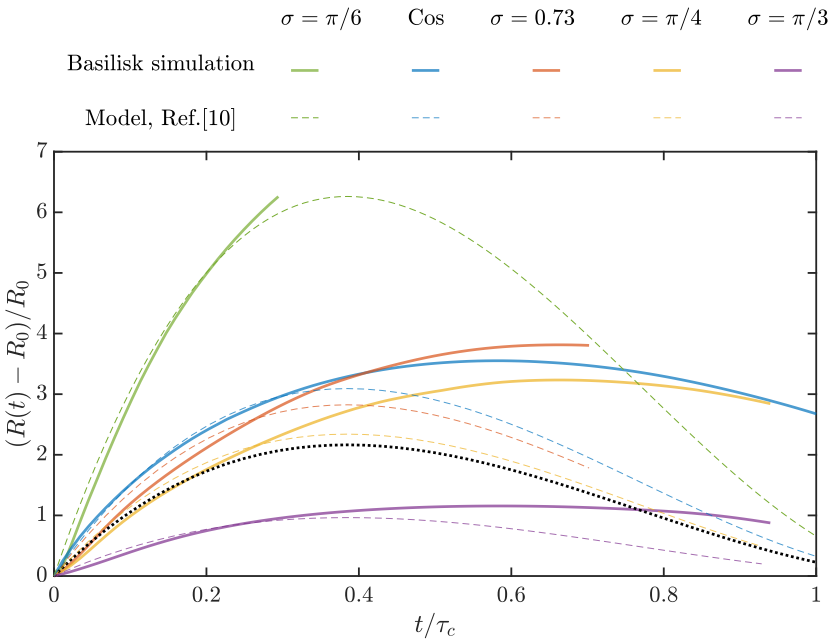

Figure A.4: Fitting the Model 1 to the different pressure profiles with data up to $0.38\tau_c$.

We	σ	u	$E_{k,d}/E_k$	$E_{k,cm}/E_k$	$E_{k,d}/E_{k,cm}$	$\widetilde{\text{We}} = \frac{\rho R_0 u^2}{\sigma}$	$\text{We}_d = \widetilde{\text{We}} E_{k,d}/E_{k,cm}$
320	$\pi/6$	0.59	0.64	0.36	1.78	249	442
320	0.73	0.49	0.35	0.65	0.54	172	92
320	$\pi/4$	0.49	0.27	0.73	0.37	172	63
320	$\pi/3$	0.47	0.06	0.94	0.06	172	11
720	cosine	0.83	0.35	0.65	0.54	488	263
320	cosine	0.54	0.35	0.65	0.54	204	110
156	cosine	0.35	0.35	0.65	0.54	90	48

Table A.1: Table with the intermediate steps to determine the breakup times. u is obtained from Fig. A.4